Journal of Process Control 122 (2023) 69–83

Contents lists available at ScienceDirect

Journal of Process Control

journal homepage: www.elsevier.com/locate/jprocont

Model complexity reduction and controller design for managed pressure drilling automation

S. Naderi Lordejani [a,c,*], B. Besselink [b], W.H.A. Schilders [c], N. van de Wouw [a,d]

[a] Department of Mechanical Engineering, Eindhoven University of Technology, The Netherlands
[b] Bernoulli Institute for Mathematics, Computer Science and Artificial Intelligence, University of Groningen, Groningen, The Netherlands
[c] Department of Mathematics and Computer Science, Eindhoven University of Technology, The Netherlands
[d] Department of Civil, Environmental and Geo-Engineering, University of Minnesota, USA

ARTICLE INFO

Article history:
Received 13 October 2021
Received in revised form 6 November 2022
Accepted 25 November 2022
Available online xxxx

Keywords:
Drilling
Model reduction
Control
Automation
Time delay systems

ABSTRACT

Automation of Managed Pressure Drilling (MPD) allows for fast and accurate pressure control in drilling operations. The achievable performance in automated MPD with model-based controllers is determined by the controller and, indirectly, also by the hydraulics model used for controller synthesis. On the one hand, such a hydraulics model should accurately capture essential flow dynamics of the system such as, e.g., wave propagation effects, for which typically complex models are needed. On the other hand, a suitable model should be simple enough to facilitate high-performance controller design as well as to support fast simulation studies supporting well scenario analysis. This paper shows that low-order models in terms of delay differential equations can effectively meet these requirements. Moreover, we propose a data-based model reduction technique to construct these low-order delay models. Next, based on this reduced-complexity model, a novel controller is designed to regulate the downhole pressure. Simulation results confirm that this controller outperforms existing pressure controllers in realistic drilling scenarios related to the mitigation of liquid kicks and mud losses encountered when drilling into high- or low-pressure zones.

1. Introduction

Energy resources such as oil and gas are often trapped within deep layers of the earth's crust. Deep wells need to be drilled to access these resources. In the drilling process of a well, a liquid, called drilling mud, is pumped in the wellbore to transport drilling cuttings to the surface and to enable the adjustment of the wellbore pressure. Specifically, the pressure at the bottom of the well should ideally be maintained at the pressure in the formations/reservoir surrounding the wellbore. This crucial requirement is related to the desire to prevent kicks, that is, unwanted flow of gas and liquid from the formation/reservoir into the wellbore, or to avoid fracturing the formation and prevent lost mud circulation, which can potentially cause a pressure drop if not addressed in time. Kicks can grow into catastrophic well control events [1] such as the Deepwater Horizon blowout [2] (for a list of other serious blowouts, see [3]).

Downhole pressure control is conventionally practiced by adjusting the mud density during drilling. However, this method of pressure control is slow and inaccurate, while also lacking a means of compensating for transient pressure fluctuations caused by, for instance, drilling into a high pressure zone and heave motions [4]. To overcome these shortcomings of the conventional pressure control method, the method of managed pressure drilling (MPD) has been introduced, see, e.g., [5,6]. In MPD, the annulus is sealed off at the surface with a rotating control device and the mud is circulated out of the well through a choke valve, see Fig. 1. This combination provides a back-pressure that can be actively controlled by changing the choke opening. Nowadays, the use of automatic control solutions is becoming more common in the automation of rotary drilling processes [7]. In particular in automated MPD, the choke valve, thereby the back-pressure, is controlled by an automatic pressure control system [6–8]. The performance of this control system depends on the pressure controller, which, in turn, is typically based on an underlying hydraulics model. This model should be accurate enough to capture the essential hydraulic characteristics of the system. At the same time, the complexity of the model should be restricted to facilitate the application of established system-theoretic analysis and controller design techniques.

Available low-complexity hydraulics models, such as the model in [8,9], are, however, incapable of capturing essential transient dynamics, such as the wave propagation effect (also known as the waterhammer effect). Ignoring such phenomena in modeling and controller design can bring about a failure in the

* Corresponding author.
E-mail address: s.naderilordejani@tue.nl (S. Naderi Lordejani).

https://doi.org/10.1016/j.jprocont.2022.11.012
0959-1524/© 2022 Published by Elsevier Ltd.

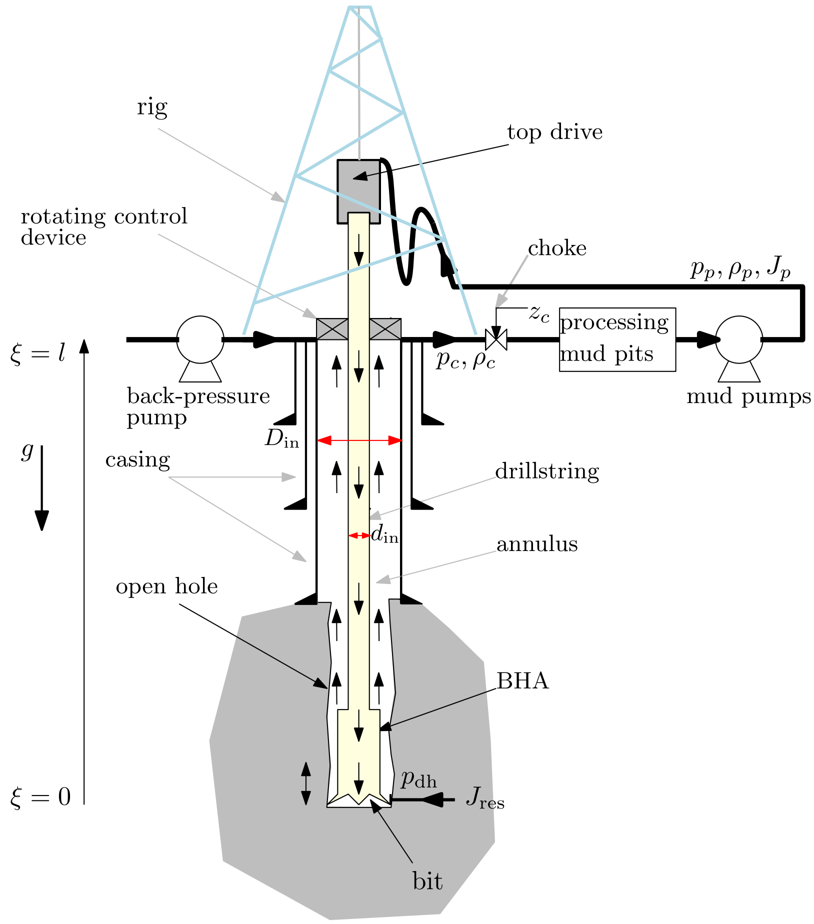

Fig. 1. A simplified schematic diagram of a drilling system operated using MPD.

accomplishment of pressure control objectives [10], such as guaranteeing that the downhole pressure remains within a safe bound around its reference value. In particular, in the case of longer wells (longer than 4000 m), the wave propagation effect becomes so significant [11] that instability issues can arise [10] when this effect is not properly taken into account during controller synthesis.

As discussed in [12], pressure control systems for MPD are conventionally designed to be slow to, among other things, avoid such stability issues. As such, these controllers are also slow in kick and mud loss attenuation. Furthermore, fast control action by these controllers can initiate undesirable propagating pressure waves which are harmful and can damage the drilling equipment. The goal of this paper is to show that a pressure control system designed based on a new low-complexity model which captures accurately the wave propagation effect can outperform conventional pressure controllers.

For many drilling scenarios, the system hydraulics can be described by linear hyperbolic partial differential equations (PDEs) and a set of boundary equations. The equations describing these boundary conditions are nonlinear, but these nonlinearities act only locally, i.e., at the boundaries. However, system analysis and controller design techniques developed for this type of PDE models are still relatively elementary and mostly focus on stabilization aspects rather than control performance. Namely, the complexity of these models currently hampers the design of controllers that can meet more advanced performance criteria.

As an approach to address complexities associated to these PDE models, model reduction techniques have gained popularity in MPD automation in the last two decades. In [8,13–15], low-order approximative models in terms of ordinary differential equations (ODEs), obtained by ignoring the distributed nature of the hydraulics of a drilling system, have been proposed and used for pressure controller design. Low- to medium-resolution spatial discretization is another model reduction approach which has been pursued in drilling automation [10,14,16,17]. A recently developed approach to constructing low-order, but accurate, hydraulics models is to apply automatic model order reduction techniques to the models resulted from the high-resolution spatial discretization [12,18,19]. A new perspective to this problem has been presented in our recent preliminary work [20], the rationale of which is explained next.

We known that the boundary input–output behavior of hyperbolic PDE systems without source terms can exactly be described by models in terms of delay-difference equations [21], also known as continuous-time difference equations (CTDEs). A well-known example is D'Alembert's formula which represents a transformation between the wave equation and delay-difference equations [22]. The presence of coupling source terms, however, leads to integro-difference systems with complex kernel functions [23]. The complexity of these kernel functions brings into question the potential of such models for controller synthesis. The work in [24] ignored the coupling source terms to obtain a delay-difference model. This model was used to design a pressure controller for the rejection of heave-induced pressure fluctuations. Contrary to [23], in [20], we have used approximations to avoid the occurrence of distributed delay terms and kernel functions. Namely, we have shown that a special class of hyperbolic PDE systems with coupling source terms can effectively be approximated by a combination of low-order models in terms of CTDEs and ODEs. In this paper, we exploit the fact that PDE models developed for single-phase flow drilling scenarios fall also into that class of models and propose to design pressure controllers on the basis of such low-complexity models.

The main contributions of this paper are as follows. First, we build upon our previous results in [20] and construct a low-order hydraulics time-delay model which is highly accurate in modeling single-phase hydraulics in MPD systems in general and liquid kicks scenarios in particular. The latter aspect is the essential novelty with respect to [20]. Second, we exploit the properties of this model and design a novel model-based pressure controller on its basis. The controller uses only the surface pressure measurements that are available in practice. To be able to design this controller, we have extended existing controller design techniques for singular time-delay system, which forms part of the theoretical contribution of this paper. Given the fact that the proposed model accurately captures the wave propagation effect, the developed controller, as opposed to conventional pressure controllers, comes with robustness against this effect. Thanks to this robustness, the controller can be tuned for fast transient performance without encountering stability issues due to the wave propagation effect. Indeed, if tuned appropriately, the presented controller can even attenuate pressure fluctuations generated due to the wave propagation effect, by virtue of the internal model principle. The effectiveness of the proposed reduced-complexity modeling and controller design strategy is evidenced by means of a simulation-based study of real-life drilling scenarios.

Outline. Section 2 is devoted to the mathematical modeling of single-phase flow (managed pressure) drilling systems. In Section 3, the proposed model complexity reduction procedure is described. The controller design technique is presented in Section 4. Simulation results are presented in Section 5 and, finally, conclusions in Section 6.

Notation. The notation $\mathbb{R}$ and $\mathbb{C}$ refer to the field of real and complex numbers, respectively. The space of all absolutely continuous functions that map the interval $[a, b]$ into $\mathbb{R}^n$ is shown by $\mathcal{C}([a, b], \mathbb{R}^n)$. A block-diagonal matrix with $A_1, \ldots, A_m$ on the diagonal is represented as $\mathrm{blkdiag}\{A_1, \ldots, A_m\}$, and I_m is the $m \times m$ identity matrix.

2. Mathematical modeling for MPD

For many drilling scenarios, a drilling system with MPD can be described by a system of linear PDEs with nonlinear boundary conditions [25]. In particular, to model the hydraulics of a drilling system, we use the so-called U-tube modeling approach. In this approach, the drilling system is modeled as two connected pipes which respectively model the drillstring and annulus of the drilling system, see Fig. 1. The flow behavior in each of these pipes is then modeled by a set of isothermal Euler equations [26], [8] of the following form (see [12] and [8] and references therein):

$$\begin{aligned} &\frac{\partial \rho_i}{\partial t} + \frac{\partial \rho_i v_i}{\partial \xi} = 0, \\ &\frac{\partial \rho_i v_i}{\partial t} + \frac{\partial p_i}{\partial \xi} = -\rho_i g \sin\theta_i - \frac{32\mu_i \rho_i v_i}{\rho_0 d_i^2}, \quad i = \mathrm{a}, \mathrm{d}, \end{aligned} \tag{1}$$

where subscripts a and d are used to distinguish between, respectively, the annulus and drillstring and their respective variables and parameters. Here, $\xi \in [0, l]$ and $t \geq 0$ are the spatial and temporal variables, respectively, l [m] is the length of the well, and $\rho_i(t, \xi)$ [kg/m^3], $v_i(t, \xi)$ [m/s] and $p_i(t, \xi)$ [Pa] represent the fluid density, velocity and pressure, respectively. Moreover, θ_i [rad], μ_i [Pa s], d_i [m] and g [m/s^2] represent the well inclination, viscosity of mud, hydraulic diameter and gravitational acceleration, respectively, and ρ_0 is the density that is measured at the reference pressure p_0. For the drillstring, $d_\mathrm{d} = d_\mathrm{in}$, where d_in is the inner diameter of the drillstring. The hydraulic diameter of the annulus is given by $d_\mathrm{a} = D_\mathrm{in} - d_\mathrm{o}$, where D_in is the wellbore diameter and d_o is the outer diameter of the drillstring. Moreover, $\theta_\mathrm{a} = -\theta_\mathrm{d}$. In this formulation, the pressure is related to the density through a linear equation of state as

$$p_i = c_l^2 (\rho_i - \rho_0) + p_0, \tag{2}$$

where c_l is the speed of sound.

The boundary conditions of this system are given by the equations describing the bit model, mass conservation over the bit, choke and pump, and read [27,28]

$$\begin{aligned} A_\mathrm{d}\eta_\mathrm{d}(t, l) - A_\mathrm{nz} c_d c_l \sqrt{2\rho_\mathrm{d}(t, l)(\rho_\mathrm{d}(t, l) - \rho_\mathrm{dh}(t))} &= 0, \\ A_\mathrm{d}\eta_\mathrm{d}(t, l) - A_\mathrm{a}\eta_\mathrm{a}(t, 0) + J_\mathrm{res}(t) &= 0, \\ A_\mathrm{a}\eta_\mathrm{a}(t, l) - k_c c_l G(z_c(t)) \sqrt{2\rho_c(t)(\rho_c(t) - \rho_0)} &= 0, \\ A_\mathrm{d}\eta_\mathrm{d}(t, 0) - J_p(t) &= 0, \end{aligned} \tag{3}$$

respectively. Herein, $\eta_i := \rho_i v_i$ is the momentum, and $\rho_\mathrm{dh}(t) := \rho_\mathrm{a}(t, 0)$ and $\rho_c(t) := \rho_\mathrm{a}(t, l)$ are the downhole and choke densities, respectively, whereas A_d [m^2], A_a [m^2], A_nz [m^2], c_d [-] and k_c [m^2] are the area of the drillstring, area of the annulus, area of the bit nozzles, discharge coefficient of the bit nozzles and the flow factor of the choke. Furthermore, J_p [kg/s], z_c [-] and $G(\cdot)$ are, respectively, the pump mass flow rate, the choke opening and the choke characteristic, which is a non-decreasing function. Moreover, J_res is the flow exchange between the reservoir and wellore, and it is described by the reservoir model. In this paper, we use the following reservoir model:

$$J_\mathrm{res}(t) = k_\mathrm{res} c_l^2 \left(\rho_\mathrm{res}(t) - \rho_\mathrm{dh}(t)\right), \tag{4}$$

where k_res [ms] is the production index of the reservoir and ρ_res is the density corresponding to the reservoir pressure p_res. In this formulation of the boundary conditions, a kick and lost circulation take place when $J_\mathrm{res} > 0$ and $J_\mathrm{res} < 0$, respectively. In an MPD configuration, the main control inputs are the pump flow rate J_c and the choke opening z_c, while ρ_res can be considered as a disturbance input.

Remark 1. It is noted that the presented model is meant to capture those dynamical aspects of a drilling system which play a significant role, from a systems and control perspective, in the overall dynamical behavior of the system for small variations in the pump flow rate. Therefore, less significant effects such as those related to rock cuttings, slow temperature transients and the rotation of the drillstring have been ignored in the model. Nonetheless, it should be mentioned that some of these effects can to a good extent be lumped into the parameters of the current model. For instance, the nonlinear behavior of the flow in the drillstring, especially in the bottom hole assembly, can with a good accuracy be included in the pressure drop across the bit [27].

Next, we write (1) in perturbation coordinates $\tilde{\rho}_i(t, \xi) = \rho_i(t, \xi) - \rho_i^*(\xi)$, $\tilde{\eta}_i(t, \xi) = \eta_i(t, \xi) - \eta_i^*(\xi)$, $i = \mathrm{a}, \mathrm{d}$, with respect to the steady-state solution ρ_i^*, η_i^*, $i = \mathrm{a}, \mathrm{d}$, that corresponds to the nominal (input and disturbance) values z_c^*, J_p^* and ρ_res^*. This change of coordinates leads to the following PDE model:

$$\frac{\partial Q}{\partial t} + \Psi_c \frac{\partial Q}{\partial \xi} + F_c Q = 0, \quad Q(0, \xi) = 0, \tag{5}$$

where $Q^T(t, \xi) = [q_\mathrm{d}^T(t, \xi), q_\mathrm{a}^T(t, \xi)]$ is the vector of distributed variables in the perturbation coordinates with $q_\mathrm{d}^T = [\tilde{\rho}_\mathrm{d}, \tilde{\eta}_\mathrm{d}]$ and $q_\mathrm{a}^T = [\tilde{\rho}_\mathrm{a}, \tilde{\eta}_\mathrm{a}]$ being the vectors of the perturbed distributed variables in the drillstring and annulus, respectively. Moreover, we have $\Psi_c = \mathrm{blkdiag}\{\Psi, \Psi\}$ and $F_c = \mathrm{blkdiag}\{F_\mathrm{d}, F_\mathrm{a}\}$, where

$$\Psi = \begin{bmatrix} 0 & 1 \\ c_l^2 & 0 \end{bmatrix}, \quad F_i = \begin{bmatrix} 0 & 0 \\ g \sin\theta_i & \frac{32\mu_i}{\rho_0 d_i^2} \end{bmatrix}. \tag{6}$$

In the perturbation coordinates, the boundary conditions (3) can be written in a vector form as follows:

$$\Pi_1 \begin{bmatrix} Q(t,0) \\ Q(t,l) \end{bmatrix} - \Pi_2 \psi \left(\Gamma \begin{bmatrix} Q(t,0) \\ Q(t,l) \end{bmatrix}, u_d(t) \right) = 0, \tag{7}$$

where $u_d \in \mathbb{R}^p$ is the vector of exogenous (perturbed) inputs, including control input and disturbance, and ψ is in general a nonlinear function. Moreover, $\Pi_1 \in \mathbb{R}^{4\times 8}$, $\Gamma \in \mathbb{R}^{\bar{m}\times 8}$ and $\Pi_2 \in \mathbb{R}^{4\times \bar{p}}$ are given matrices. Here, $\bar{m}$ is the dimension of the first argument of ψ and $\bar{p}$ is the dimension of this function. For details, see (47) and (48) in Appendix A. The elements of the input u_d are defined depending on the drilling scenario under consideration. In this paper, we only consider scenarios where $\tilde{J}_p = 0$ and, thus, define $u_d^T(t) = [\tilde{z}_c(t), \tilde{\rho}_{\mathrm{res}}(t)]$, where $\tilde{z}_c(t) = z_c(t) - z_c^*$ and $\tilde{\rho}_{\mathrm{res}}(t) = \rho_{\mathrm{res}}(t) - \rho_{\mathrm{res}}^*$. Furthermore, we assume that for some matrix $H \in \mathbb{R}^{m\times \bar{m}}$, the output is given by

$$y(t) = H\Gamma \begin{bmatrix} Q(t,0) \\ Q(t,l) \end{bmatrix}. \tag{8}$$

In this paper, the output is a vector of the perturbed pump, downhole and choke densities, $\tilde{\rho}_p$, $\tilde{\rho}_{\mathrm{dh}}$ and $\tilde{\rho}_c$ as defined below (3), respectively. Note that $\tilde{\rho}_c(t) = \rho_c(t) - \rho_c^*$, $\tilde{\rho}_{\mathrm{dh}}(t) = \rho_{\mathrm{dh}}(t) - \rho_{\mathrm{dh}}^*$ and $\tilde{\rho}_p(t) = \rho_p(t) - \rho_p^*$, where $\rho_p(t) = \rho_{\mathrm{d}}(t,0)$ is the mud density at the pump.

Remark 2. In (5), the term $F_c Q$ models the in-domain interactions among the components of Q and it is known as the coupling source term. We also mention that the high accuracy of such a model as in (1) and (3) has been validated in [12] by comparing it with field data from real-life MPD operations.

To facilitate the model reduction procedure of the next section, we first reformulate the model in the perturbation coordinates described by (5), (7) and (8). This model can be decomposed into a feedback interconnection of a linear subsystem and a nonlinear mapping, where the latter represents the nonlinearities in the boundary conditions. This decomposition is motivated by the fact that the nonlinearities occur in the model only locally (i.e., through the boundary conditions), and by the fact that it enables us to reduce the model complexity by only reducing the complexity of the linear PDE part and leaving the structure of the static nonlinearities intact. In particular, the system described by (5), (7) and (8) can be cast into a feedback interconnection of an infinite-dimensional linear system Σ and a nonlinear mapping $\psi(\cdot,\cdot)$ as

$$\Sigma : \begin{cases} \dfrac{\partial Q}{\partial t} + \Psi_c \dfrac{\partial Q}{\partial \xi} + F_c Q = 0, \\ Q(0,\xi) = 0, \\ \Pi_1 \begin{bmatrix} Q(t,0) \\ Q(t,l) \end{bmatrix} = \Pi_2 v(t), \\ w(t) = \Gamma \begin{bmatrix} Q(t,0) \\ Q(t,l) \end{bmatrix}, \\ y(t) = H w(t), \end{cases} \tag{9}$$

$$v(t) = \psi(w(t), u_d(t)), \tag{10}$$

where $w(t) \in \mathbb{R}^{\bar{m}}$ is the output of the infinite-dimensional part of Σ and $v(t) \in \mathbb{R}^{\bar{p}}$ is its input, see Fig. 2.

Given the system in (9), (10), the objective is to approximate the input–output behavior of this system from the input u_d to the output y with a model of a lower complexity, allowing for faster yet accurate time-domain simulations. More importantly in the scope of this paper, this model should possess a structure that facilitates the design of high-performance controllers, while still capturing the wave-propagation effects, an essencial characteristic to such hyperbolic PDEs. Considering Fig. 2, the model complexity reduction problem in this paper is pursued by approximating Σ by a model $\hat{\Sigma}$ of desirable properties, which are yet to be introduced.

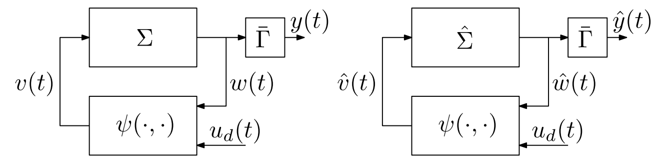

Fig. 2. A block diagram of the reformulated model: (left) before reduction, (right) after complexity reduction.

Remark 3. It is noted that the model Σ is indeed obtained by linearizing the nonlinear model (3) and (5) around an operating profile that corresponds to nominal inputs z_c^*, J_p^* and ρ_{res}^*. Constructing Σ in this way guarantees Σ to be asymptotically stable, because the single-phase flow drilling systems have inherently stable hydraulics [29].

In view of our model reduction objectives, let us now present the transfer function of Σ from v to w, i.e., of the linear, infinite-dimensional, part of the system in (9), (10).

Lemma 1. *Consider the linear system Σ in (9). The matrix transfer function $T(s)$ of this system from the input v to the output w in the Laplace domain is given by*

$$T(s) = \Gamma \begin{bmatrix} I_4 \\ e^{\Xi(s)l} \end{bmatrix} \left(\Pi_1 \begin{bmatrix} I_4 \\ e^{\Xi(s)l} \end{bmatrix} \right)^{-1} \Pi_2, \tag{11}$$

where $s \in \mathbb{C}$ is the Laplace variable and $\Xi(s) = \mathrm{blkdiag}\{\Xi_{\mathrm{d}}, \Xi_{\mathrm{a}}\}$, with the diagonal elements $\Xi_i(s) = -\Psi^{-1}(sI_2 + F_i)$, for $i \in \{\mathrm{a}, \mathrm{d}\}$.

Proof 1. The proof of this lemma can be found in Appendix B.

Remark 4. By exploiting an implication of the Cayley–Hamilton theorem, we can obtain an explicit expression of $\exp(\Xi_i(s)\xi)$, $i \in \{\mathrm{a}, \mathrm{d}\}$, in Lemma 1 is given by

$$e^{\Xi_i(s)\xi} = e^{-\alpha\xi} \begin{bmatrix} m_{11}(s,\xi) & -\frac{s+f_{22}}{c^2\beta}\sinh(\beta\xi) \\ -\frac{s+f_{11}}{\beta}\sinh(\beta\xi) & m_{22}(s,\xi) \end{bmatrix}, \tag{12}$$

with

$$m_{11}(s,\xi) = \cosh(\beta(s)\xi) + \left(\alpha - \frac{f_{21}}{c^2}\right)\frac{\sinh(\beta(s)\xi)}{\beta(s)}, \tag{13}$$

$$m_{22}(s,\xi) = \cosh(\beta(s)\xi) + (\alpha - f_{12})\frac{\sinh(\beta(s)\xi)}{\beta(s)}, \tag{14}$$

and $\beta(s) = \sqrt{\alpha^2 + (s+f_{22})(s+f_{11})/c^2 - f_{12}f_{21}/c^2}$ and $\alpha = 0.5(f_{12} + f_{21}/c^2)$, for

$$F_i = \begin{bmatrix} f_{11} & f_{12} \\ f_{21} & f_{22} \end{bmatrix}, \quad i \in \{\mathrm{a}, \mathrm{d}\},$$

in (6) and where the subscript i has been dropped from the elements of F_i for notational simplicity.

In the next section, we construct a model of reduced complexity by replacing Σ in (9) by a system of an appropriate delay structure. The latter system is constructed by matching its transfer function to that of Σ, as derived in Lemma 1.

3. Reduced-complexity time delay model

In this section, we present a data-based method for constructing the reduced-complexity model $\hat{\Sigma}$ that should approximate Σ

in (9). As a stepping stone towards this goal, we first motivate an appropriate structure for $\hat{\Sigma}$.

3.1. Model structure

If we neglect the source term in (9), that is, if we assume $F_c = 0$, the model reduces to a number of pure advection equations. It is well-known that such an advection equation is a representation of a time delay of l/c_l seconds. This implies that Σ in the absence of source terms can be modeled by a system of continuous time difference equations (CTDEs), which represent transport phenomena in hyperbolic PDE systems. Source terms, however, cause distributed in-domain couplings between the traveling waves along the spatial domain. These interactions especially affect the low-frequency behavior of the system Σ. We can show that $\exp(\Xi_i(s)l)$, $i = \{\mathrm{a}, \mathrm{d}\}$, in (11), which determine the transfer function $T(s)$ of Σ, converges to a periodic behavior of a period of $2\pi c_l/l$ at high frequencies (see Appendix C for details). The periodic behavior of $\exp(\Xi_i(j\omega)l)$, which is hence also induced in $T(j\omega)$, is a manifestation of the advective nature of the system. Thus, we conclude that in the presence of these source terms, the system behavior is composed of two dominating aspects:

- advection,
- dynamics governing the average shape of advective waves at the boundaries, which have a slow and smooth nature.

As mentioned before, the (advection-induced) transport aspects can be modeled by CTDEs. This is the dominating aspect at high frequencies. Given the fact that the second aspect has the largest contribution to the system response at low frequencies, this can be accurately modeled using a system of ODEs.

Remark 5. The ODE part is also inspired by the fact that physics-based model-complexity reduction of PDE models by ignoring the wave propagation effects leads to low-order ODE models [8]. From a physical perspective, a careful observation reveals that the output response of the PDE can be decomposed into a slow and smooth response and an (damped) oscillatory response. The CTDE is indeed responsible for capturing the oscillatory behavior while the ODE part captures the slow, smooth response and the damping effects in the oscillation.

This explanation motivates us to consider for $\hat{\Sigma}$ a structure which consists of an interconnection of a CTDE model Σ_{ctde} and an ODE model Σ_{ode}. Here, we adopt a parallel interconnection between Σ_{ctde} and Σ_{ode}, as illustrated in Fig. 3, with the following state-space realizations:

$$\Sigma_{\text{ode}} : \begin{cases} E_1\dot{x}_1(t) = A_1x_1(t) + B_1\hat{v}(t), \\ \hat{w}_1(t) = C_1x_1(t) + D_1\hat{v}(t), \end{cases} \tag{15}$$

$$\Sigma_{\text{ctde}} : \begin{cases} E_2x_2(t) = -A_2x_2(t-\tau) + B_2\hat{v}(t), \\ \hat{w}_2(t) = C_2x_2(t), \end{cases} \tag{16}$$

where $x_1(t) \in \mathbb{R}^{n_1}$, $x_2(t) \in \mathbb{R}^{n_2}$ and $\hat{w} = \hat{w}_1 + \hat{w}_2$. The state of the CTDE is given by the function segment $x_{2,t} : [-\tau, 0] \to \mathbb{R}^{n_2}$, and its initial condition is indicated by $x_{2,0} \in \mathcal{C}([-\tau, 0], \mathbb{R}^{n_2})$. We assume that the matrix E_1 in (15) is invertible.

Now, the model $\hat{\Sigma}$ can be rewritten in the following form:

$$\hat{\Sigma} : \begin{cases} E\dot{x}(t) = Ax(t) + A_dx(t-\tau) + B\hat{v}(t), \\ \hat{w}(t) = Cx(t), \end{cases} \tag{17}$$

where $x = [x_1^T, x_2^T]^T \in \mathbb{R}^n$, and

$$E = \text{blkdiag}\{I_{n_1}, 0_{n_2}\}, C = [C_1, C_2], B = [(E_1^{-1}B_1)^T, B_2^T]^T$$
$$A = \text{blkdiag}\{E_1^{-1}A_1, -E_2\}, A_\text{d} = \text{blkdiag}\{0_{n_1}, -A_2\}.$$

Next, we present a method for the construction of the realizations in (15) and (16).

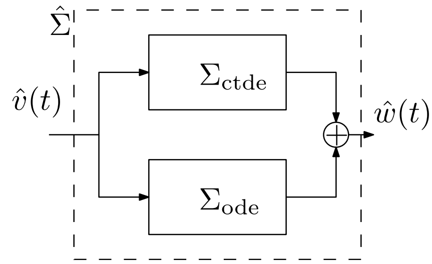

Fig. 3. A block diagram of the proposed structure for $\hat{\Sigma}$.

3.2. Data-based model construction

In this section, we introduce a method that constructs an approximating model based on an input–output description of the original system in the Laplace domain. This approach is based on the work [30,31]. It is applicable to a class of systems that can be represented by a transfer function of the form

$$\hat{T}(s) = CK^{-1}(s)B, \tag{18}$$

where $C \in \mathbb{R}^{\bar{m}\times n}$, $B \in \mathbb{R}^{n\times\bar{p}}$, and $K(s)$ comes with a general structure of the form $K(s) = \sum_{k=1}^{N} h_k(s)A_k$. Here, $\{h_1(s), \ldots, h_N(s)\}$ is a linearly independent set of functions such that $h_k : \mathbb{C} \to \mathbb{C}$ is meromorphic for $k = 1, \ldots, N$ [30]. The structured transfer function (18) represents a large class of systems. For example, the transfer function of a CTDE system (as in (16)) can be written in this form by taking $h_1(s) = 1$ and $h_2(s) = \exp(-\tau s)$, and a first-order ODE structure (as in (15)) by $h_1(s) = s$ and $h_2(s) = -1$, both for $N = 2$. The data-driven method proposed in [30] supports constructing (approximate) system models with a transfer function of the form (18) that satisfy certain interpolation conditions. To use this method, we first define which data of the transfer function $T(s)$ (to be approximated by $\hat{T}(s)$) is available. This data is obtained by evaluating $T(s)$ at certain (interpolation) points in the complex plane. It is assume that the data sets $\{\lambda_i, r_i, w_i, \mu_i, l_i, v_i\}_{i=1}^n$, for which

$$T(\lambda_i)r_i = w_i, \quad l_i^T T(\mu_i) = v_i^T, \ \ i = 1, 2, \ldots, n, \tag{19}$$

holds, are given. Here, n is the number of interpolation points, λ_i, $\mu_i \in \mathbb{C}$ are the interpolation points, $r_i \in \mathbb{C}^{\bar{p}}$, $l_i \in \mathbb{C}^{\bar{m}}$ are the right and left tangential direction vectors and $w_i \in \mathbb{C}^{\bar{m}}$, $v_i \in \mathbb{C}^{\bar{p}}$ are the corresponding system responses. The data λ_i and μ_i and directions r_i and l_i can be chosen arbitrarily provided $T(s)$ is well-defined at these points.

The approach by [30] enables us to construct a realization (18), such that its transfer function satisfies the interpolation conditions

$$\hat{T}(\lambda_i)r_i = T(\lambda_i)r_i = w_i, \tag{20}$$

$$l_i^T\hat{T}(\mu_i) = l_i^T T(\mu_i) = v_i^T, \tag{21}$$

for all $i = 1, 2, \ldots, n$. For convenience, we collect the interpolation data in a matrix form as

$$\begin{aligned} &\Lambda := \text{diag}(\lambda_1, \ldots, \lambda_n), && M := \text{diag}(\mu_1, \ldots, \mu_n), \\ &R := [r_1, \ldots, r_n], && L := [l_1, \ldots, l_n], \\ &W := [w_1, \ldots, w_n], && V := [v_1, \ldots, v_n]. \end{aligned} \tag{22}$$

Next, we present theorems which allow for the construction of realizations for Σ_{ctde} and Σ_{ode} on the basis of the interpolation data. The ODE part of the reduced realization $\hat{\Sigma}$ can be constructed using following result.

Theorem 1. *For the data in (22), let $\{\lambda_i\}_{i=1}^n \cap \{\mu_i\}_{i=1}^n = \emptyset$, and suppose that $T(s)$ is well-defined for every $s \in \{\lambda_i\}_{i=1}^n \cup \{\mu_i\}_{i=1}^n$. Moreover, let (E_1, A_1, B_1, C_1) be given by*

$$\begin{aligned} [E_1]_{i,j} &= \frac{l_i^T w_j - v_i^T r_j}{\mu_i - \lambda_j},\ i,j = 1,\dots,n,\\ [A_1]_{i,j} &= \frac{\mu_i v_i^T r_j - l_i^T w_j \lambda_j}{\lambda_j - \mu_i} + l_i^T D_1 r_j,\ i,j = 1,\dots,n,\\ B_1 &= V^T - D_1 R,\\ C_1 &= W - L^T D_1, \end{aligned} \tag{23}$$

for a given $D_1 \in \mathbb{R}^{\bar{m}\times\bar{p}}$. Then, the realization of Σ_{ode} given by (15) with transfer function

$$T_{\text{ode}}(s) = C_1\,(sE_1 - A_1)^{-1} B_1 + D_1,$$

satisfies the interpolation conditions in (20) and *(21).*

Proof 2. This theorem presents a specific case of results in [30], where a detailed proof can be found.

Likewise, the result in the next theorem allows for the construction of the CTDE part Σ_{ctde} of the approximate model.

Theorem 2. *For the data in (22), let $\{\lambda_i\}_{i=1}^n \cap \{\mu_i\}_{i=1}^n = \emptyset$, and suppose that $T(s)$ is well-defined for every $s \in \{\lambda_i\}_{i=1}^n \cup \{\mu_i\}_{i=1}^n$. Moreover, let (E_2, A_2, B_2, C_2) be given by*

$$\begin{aligned} [E_2]_{i,j} &= \frac{e^{-\tau\mu_i} v_i^T r_j - l_i^T w_j e^{-\tau\lambda_j}}{e^{-\tau\mu_i} - e^{-\tau\lambda_j}},\ i,j = 1,\dots,n,\\ [A_2]_{i,j} &= \frac{v_i^T r_j - l_i^T w_j}{e^{-\tau\lambda_j} - e^{-\tau\mu_i}},\ i,j = 1,\dots,n,\\ B_2 &= V^T,\\ C_2 &= W. \end{aligned} \tag{24}$$

Then, the realization Σ_{ctde} given by (16) with the transfer function

$$T_{\text{ctde}}(s) = C_2\left(E_2 + e^{-\tau s} A_2\right)^{-1} B_2,$$

satisfies the interpolation conditions in (20) and *(21).*

Proof 3. This theorem presents a special case of results in [30], where a detailed proof can be found.

Remark 6. The data matrices M, Λ, V, W, L, R and the order n in Theorem 2 are not the same as those in Theorem 1, although this may appear to be the case because of the abuse of notation. Indeed, we have two distinct sets of data. In particular, M^1, Λ^1, V^1, W^1, L^1, R^1 and n_1 will denote the interpolation data that are used for the ODE part, and M^2, Λ^2, V^2, W^2, L^2, R^2 and n_2 contain the interpolation data used for the construction of Σ_{ctde} using Theorem 2.

The procedure for constructing the reduced model $\hat{\Sigma}$ is detailed in Algorithm 1. This algorithm first constructs a realization for Σ_{ctde} from transfer function data of the original PDE model, while choosing the interpolation points in the high-frequency range. Namely, the PDE dynamics are well approximated by the CTDE in that range, see Section 3.1. Next, given Σ_{ctde}, Σ_{ode} is constructed such that it approximates the difference between $T(s)$ and $T_{\text{ctde}}(s)$ in the low-frequency range.

Remark 7. The feedthrough matrix D_1 in Theorem 1 is set to 0 in Algorithm 1. This makes it possible for the relation $\lim_{\omega\to\infty} T(j\omega) = T_{\text{ctde}}(j\omega)$ to hold, following the fact that $\lim_{\omega\to\infty} T_{\text{ode}}(j\omega) = D_1$.

Algorithm 1: Construction of Σ_{ctde} and Σ_{ode}

Input: M^1, Λ^1, L^1, R^1, D_1, M^2, Λ^2, V^2, W^2, L^2, R^2, and $T(s)$ in (11)

Output: Realizations $(E_1, A_1, B_1, C_1, D_1)$ and (E_2, A_2, B_2, C_2) for Σ_{ode} and Σ_{ctde}

1. Construct (E_2, A_2, B_2, C_2) and $T_{\text{ctde}}(s)$ from M^2, Λ^2, V^2, W^2, L^2 and R^2 using Theorem 2.
2. For $T(s)$ as in (11), compute the error transfer function $T_{\text{e}}(s) := T(s) - T_{\text{ctde}}(s)$.
3. Compute W^1 and V^1 based on $T_{\text{e}}(s)$ from M^1, Λ^1, R^1 and L^1.
4. Construct(E_1, A_1, B_1, C_1) and $T_{\text{ode}}(s)$ using Theorem 1 by interpolating $T_{\text{e}}(s)$ for M^1, Λ^1, V^1, W^1, L^1, R^1 and D_1.

Remark 8. Choosing the optimal location of the interpolation points in Algorithm 1 is beyond the scope of this paper. Nonetheless, we employ Algorithm 1 itself inside another minimization algorithm to optimally locate the interpolation points. The cost function of this minimization problem is a weighted, frequency-limited H_2-norm, and the region of the complex plane where the interpolation points can lay in is specified in that algorithm. The algorithm also enforces the exponential stability of the reduced system $\hat{\Sigma}$ by constraints on the eigenvalues of $E_1^{-1}A_1$ and $-E_2^{-1}A_2$.

Remark 9. Even though the interpolation points can take real parts, we chose to restrict those to the imaginary axis only. This keeps the possibility open to construct Σ_{ctde} and Σ_{ode} from frequency response data obtained from real-life measurements.

In summary, we have exploited properties of CTDE and ODE models to construct a low-order, accurate hydraulics model for MPD scenarios. In this model, the CTDE part is primarily responsible for capturing the wave propagation effects, while the ODE part improves the approximation accuracy in the low frequency range, by compensating for effects of the coupling source terms and capturing the slow dynamics of the system. The effectiveness of this model approximation approach is illustrated in Section 5.1. In the next section, we use this low-order delay model to design a pressure control system for drilling scenarios.

4. Pressure controller design

In this section, we use the reduced-complexity delay model to design a pressure control system to prevent/attenuate liquid kicks by appropriately controlling the downhole pressure p_{dh}. Hereto, a Lyapunov–Krasovskii design approach for descriptor time-delay systems is taken.

Let us first rewrite $\hat{\Sigma}$ in (17) in a more tractable form

$$\hat{\Sigma}:\begin{cases} E\dot{x}(t) = Ax(t) + A_{\text{d}}x(t-\tau) + B_u u(t) + B_d d(t),\\ y_{\text{m}}(t) = C_{\text{m}}x(t),\\ y_{\text{p}}(t) = C_{\text{p}}x(t), \end{cases} \tag{25}$$

where $u = \hat{v}_1$ is the control input and $d = \hat{v}_2$ is an unknown disturbance to the system (with $\hat{v}^T = [\hat{v}_1, \hat{v}_2]$ in (17)). We recall that d is the perturbed reservoir density $\tilde{\rho}_{\text{res}}$. Moreover, B_u and B_d are the relevant parts of B in (17). Furthermore, y_{m} is the measured output (measured at the surface), while the unmeasured signal y_{p} is the performance output, and C_{m} and C_{p} are the relevant parts of C in (17). It is noted that y_{m} contains the perturbed (approximate) pump and choke densities whereas y_{p} is the perturbed downhole density.

The primary control objective is to design u such that $\lim_{t\to\infty}(y_{\text{p}}(t) - d(t)) = 0$, while ensuring stability of the closed-loop system. Moreover, the controller should satisfy some performance energy measure. Following the linear reservoir model in

(4), this objective ensures the attenuation of liquid kicks and lost mud circulations.

Remark 10. We note that $u = \hat{v}_1$ is a virtual control input, and after designing it, we need to convert it into the physical input $\tilde{z}_c$ (related to choke actuation). For this, we use the fact that $u = \psi_1(y_{\mathrm{m}}, \tilde{z}_c)$ to design $\tilde{z}_c$ (ψ_1 is the first element of ψ). Following the definition of ψ in Appendix A, we obtain

$$\tilde{z}_c(t) = \frac{\sqrt{2\rho_c^*\left(\rho_c^* - \rho_0\right)\left(u + z_c^* - T_{37}y_{\mathrm{m},2}(t)\right)}}{\sqrt{2\left(y_{\mathrm{m},2}(t) + \rho_c^*\right)\left(y_{\mathrm{m},2}(t) + \rho_c^* - \rho_0\right)}} - z_c^*,$$

where it is recalled that $y_{\mathrm{m},2}$ is the measured perturbed choke density $\tilde{\rho}_c$ and T_{37} is as in (46). To simplify the controller design procedure, we have discarded the effects of the bit-induced nonlinearities in ψ on $\hat{\Sigma}$, i.e., ψ_3 and its corresponding inputs and outputs have been omitted from the model. This is justified by the assumption of fixed pump flow, which makes the effects of this nonlinearity insignificant.

Now, we make the following realistic assumption resembling the scenario of suddenly running into high- or low-pressure zones while drilling ahead.

Assumption 1. The reservoir density $d(t)$ is a piecewise constant function of time.

4.1. Feedforward controller

Given the fact that the open-loop system is asymptotically stable, we start with the design of a feedforward controller, assuming momentarily that $d(t)$ is known. This controller should have the following structure:

$$u(t) = K_{\mathrm{ff}}d(t), \tag{26}$$

where K_{ff} is the feedforward control gain. To design this gain, we consider the equilibrium equation (associated to (25)):

$$0 = (A + A_{\mathrm{d}})x^* + B_u u^* + B_d d, \tag{27}$$

where the star $*$ indicates the variables at the equilibrium point for $d(t) = d$, with d constant (note that for $d \neq 0$, the steady-state solution of (25) is not zero anymore). If $A + A_{\mathrm{d}}$ is nonsingular, for x^*, we obtain

$$x^* = -(A + A_{\mathrm{d}})^{-1}\left(B_u u^* + B_d d\right). \tag{28}$$

The substitution of x^* from (28) into the equation of the performance output in (25) yields

$$y_{\mathrm{p}}^* = -C_{\mathrm{p}}(A + A_{\mathrm{d}})^{-1}\left(B_u u^* + B_d d\right).$$

Given the control objective, which is $y_p^* = d$, we obtain

$$d = -C_{\mathrm{p}}(A + A_{\mathrm{d}})^{-1}\left(B_u u^* + B_d d\right).$$

Finally, we can solve this equation for u^* to obtain $u^* = K_{\mathrm{ff}}d$, which leads to

$$K_{\mathrm{ff}} = -\frac{1 + C_{\mathrm{p}}(A + A_{\mathrm{d}})^{-1}B_d}{C_{\mathrm{p}}(A + A_{\mathrm{d}})^{-1}B_u}. \tag{29}$$

Remark 11. The feedforward controller requires that the steady-state gain $C_{\mathrm{p}}(A + A_{\mathrm{d}})^{-1}B_u$ to be nonzero (note that this is a scalar term). From a physical perspective, this requirement is met, because any change in the input z_c^* leads to a change in p_{dh}^* in practice. Moreover, the regularity of the matrix $A + A_{\mathrm{d}}$ is guaranteed by the asymptotic stability of the reduced system, which is enforced by the model reduction algorithm, see Remark 8.

4.2. State-feedback control

In practice, we are interested in the transient response of the system as well. For this reason, we extend the controller in (26) with a state-feedback term, leading to a control law of the form

$$u(\tilde{x}) = -K_{\mathrm{sf}}\tilde{x}(t) + K_{\mathrm{ff}}d, \quad \tilde{x} = x - x^*, \tag{30}$$

where x^* is given in (28) and K_{sf} is the state-feedback gain, yet to be designed. Later, we will design an observer that reconstructs $\tilde{x}$ from measured data.

Let us now study properties of the closed-loop system resulting from the control law (30). The closed-loop dynamics are obtained by substituting this control law into (25):

$$E\dot{\tilde{x}}(t) = A_c\tilde{x}(t) + A_{\mathrm{d}}\tilde{x}(t-\tau) + (A + A_{\mathrm{d}})\,x^* + (B_u K_{\mathrm{ff}} + B_d)\,d,$$

with $A_c = A - BK_{\mathrm{sf}}$. The use of (27) implies that

$$E\dot{\tilde{x}}(t) = A_c\tilde{x}(t) + A_{\mathrm{d}}\tilde{x}(t-\tau), \tag{31}$$

which represents the closed-loop (time-delay) dynamics. The feedback gain K_{sf} should be designed such that the closed-loop dynamics (31) have a desirable transient performance while it is guaranteed to be asymptotically stable. Hereto, we present the following result.

Theorem 3. *Let there exist symmetric, positive definite matrices P_1 and U, and matrices P_2 and $\bar{K}$, an invertible matrix P_3, and a scalar α_c such that*

$$\begin{bmatrix} \Phi_{11} & * & * & * & * \\ \Phi_{21} & \Phi_{22} & * & * & * \\ \tau\Lambda\left(AP - B\bar{K}\right) & \tau\Lambda A_{\mathrm{d}}P & -\alpha_c^{-1}P_1 & * & * \\ Q_h P & 0 & 0 & -I_q & * \\ \gamma\bar{K} & 0 & 0 & 0 & -I_p \end{bmatrix} < 0, \tag{32}$$

with $\Phi_{11} = P^TA^T + AP + U - \bar{K}^TB^T - B\bar{K} - \alpha_c\Lambda^TP_1\Lambda$, $\Phi_{21} = P^TA_{\mathrm{d}}^T + \alpha_c\Lambda^TP_1\Lambda$ and $\Phi_{22} = -U - \alpha_c\Lambda^TP_1\Lambda$, holds for a given matrix Q_h, a given scalar γ, $\Lambda = [I_{n_1}, 0_{n_1\times n_2}]$ and

$$P = \begin{bmatrix} P_1 & 0 \\ P_2 & P_3 \end{bmatrix}.$$

Then, for $K_{\mathrm{sf}} = \bar{K}P^{-1}$, the closed-loop system dynamics (31) is asymptotically stable. Moreover, the inequality

$$\int_t^{\infty}\left(\tilde{x}^T(t)Q_h^TQ_h\tilde{x}(t) + \gamma^2u_{\mathrm{sf}}^2(t)\right)\,dt < V_c(\tilde{x}_t), \tag{33}$$

holds. Here, $u_{\mathrm{sf}} = -K_{\mathrm{sf}}\tilde{x}$, and the functional V_c reads

$$\begin{aligned} V_c(\tilde{x}_t) &= \tilde{x}^T(t)E\bar{P}\tilde{x}(t) + \int_{t-\tau}^{t}\tilde{x}^T(s)\bar{U}\tilde{x}(s)ds \\ &\quad + \tau\alpha_c\int_{t-\tau}^{t}\int_{\theta}^{t}\dot{\tilde{x}}_1^T(s)\bar{P}_1\dot{\tilde{x}}_1(s)\,dsd\theta, \end{aligned} \tag{34}$$

with $\bar{P} = P^{-1}$, $\bar{P}_1 = P_1^{-1}$ and $\bar{U} = P^{-T}UP^{-1}$.

Proof 4. The proof can be found in Appendix D.

Indeed, (33) is our performance measure for control. Here, Q_h and γ are design parameters that enable us to influence the transient response of the closed-loop system. In general, a larger γ, being a weight on the control action, leads to a smaller control signal $u_{\mathrm{sf}}(t)$ while a large Q_h, being a weight on the transient response, makes the closed-loop system response faster. This tradeoff can be understood by realizing that the cost function in the left-hand side of (33) is heuristically minimized by tightening and minimizing its upper bound $V_c(\tilde{x}_0)$. As a computationally tractable heuristic for minimizing $V_c(\tilde{x}_0)$, we minimize the trace of P_1^{-1}.

4.3. Observer design

Clearly, the control law (30) is not implementable in practice because the states $\tilde{x}$ are neither measurable nor have a clear physical meaning. For this reason, we next design an observer-based, state-feedback controller, which only requires the output measurements $y_{\rm m}$. The corresponding control law has the following form:

$$u(t) = -K_{\rm sf}(\hat{x}(t) - x^*) + K_{\rm ff}\hat{d}(t), \tag{35}$$

where $\hat{x}(t)$ and $\hat{d}(t)$ are estimates for $x(t)$ and d, respectively. These estimates are obtained from the following observer:

$$\begin{cases} \dot{\hat{d}}(t) = L_1\left(y_{\rm m}(t) - \hat{y}_{\rm m}(t)\right), \\ E\dot{\hat{x}}(t) = A\hat{x}(t) + A_{\rm d}\hat{x}(t-\tau) + B_u u(t) + B_d\hat{d}(t) \\ \qquad + L_2\left(y_{\rm m}(t) - \hat{y}_{\rm m}(t)\right), \\ \hat{y}_{\rm m}(t) = C_{\rm m}\hat{x}(t), \\ \hat{y}_{\rm p}(t) = C_{\rm p}\hat{x}(t), \end{cases} \tag{36}$$

where L_1 and L_2 are the observer gains to be designed.

Now, we study the closed-loop system dynamics (25), (35) and (36). To this end, we define $e := x - \hat{x}$ and $e_d := d - \hat{d}$, and obtain the error dynamics

$$\begin{aligned} &\dot{e}_d(t) = -L_1 C_{\rm m} e(t), \\ &E\dot{e}(t) = (A - L_2 C_{\rm m})\, e(t) + A_{\rm d} e(t-\tau) + B_d e_d(t), \end{aligned} \tag{37}$$

where we have used $\dot{d} = 0$ from Assumption 1. Now, we rewrite the input as $u = -K_{\rm sf}\tilde{x} + K_{\rm ff}d + K_{\rm sf}e - K_{\rm ff}e_d$. Substituting this into (25) and using (27) leads to

$$\begin{aligned} E\dot{\tilde{x}}(t) = (A - B_u K_{\rm sf})\tilde{x}(t) + A_{\rm d}\tilde{x}(t-\tau) \\ + B_u K_{\rm sf} e(t) - B_u K_{\rm ff} e_d(t). \end{aligned} \tag{38}$$

The (error) dynamics in (37) and (38) can be written as

$$\begin{aligned} \begin{bmatrix} E\dot{\tilde{x}}(t) \\ E\dot{e}(t) \\ \dot{e}_d(t) \end{bmatrix} &= \begin{bmatrix} A - B_u K_{\rm sf} & B_u K_{\rm sf} & -B_d K_{\rm ff} \\ 0 & A - L_2 C_{\rm m} & B_d \\ 0 & -L_1 C_{\rm m} & 0 \end{bmatrix} \begin{bmatrix} \tilde{x}(t) \\ e(t) \\ e_d(t) \end{bmatrix} \\ &+ \begin{bmatrix} A_d & 0 & 0 \\ 0 & A_d & 0 \\ 0 & 0 & 0 \end{bmatrix} \begin{bmatrix} \tilde{x}(t-\tau) \\ e(t-\tau) \\ e_d(t-\tau) \end{bmatrix}. \end{aligned}$$

This formulation of the closed-loop dynamics clearly illustrates a type of separation principle, implying that the exponential stability of the error dynamics in (37) guarantees the exponential stability of the closed-loop system. We exploit this fact to design L_1 and L_2 independently of $K_{\rm sf}$. By defining $z^T := [e_d, e^T]$, (37) can be written in the form

$$\bar{E}\dot{z}(t) = \left(\bar{A} - L\bar{C}\right) z(t) + \bar{A}_{\rm d} z(t-\tau), \tag{39}$$

where $\bar{E} = \text{blkdiag}\{1, E\}$, $\bar{A}_d = \text{blkdiag}\{0, A_d\}$ and

$$\bar{A} = \begin{bmatrix} 0 & 0 \\ B_d & A \end{bmatrix}, L = \begin{bmatrix} L_1 \\ L_2 \end{bmatrix}, \bar{C} = \begin{bmatrix} 0 & C_{\rm m} \end{bmatrix}.$$

We have the following statement on the stability of (39).

Theorem 4. *Consider the error dynamics (39) of the observer. Let there exist matrices Q_2 and Q_3, a nonsingular matrix S, and positive definite, symmetric matrices H, M and Q_1, and a scalar α_o for which*

$$\begin{bmatrix} \Theta_{11} & * & * \\ \bar{A}_{\rm d}^T S^T + \bar{M} & -H - \bar{M} & * \\ Q - S^T + \alpha_o S\bar{A} - \alpha_o \bar{L}\bar{C} & \alpha_o S\bar{A}_{\rm d} & \Theta_{33} \end{bmatrix} < 0, \tag{40}$$

with $\Theta_{11} = S\bar{A} + \bar{A}^T S^T + H - \bar{M} - \bar{L}\bar{C} - \bar{C}^T\bar{L}^T + Q_o$, $\Theta_{33} = -\alpha_o\left(S + S^T\right) + \tau^2\bar{M}$ and $\bar{M} = \Lambda^T M \Lambda$, holds for a given matrix $Q_o = Q_o^T \geq 0$. Then, for $L = S^{-1}\bar{L}$, the error dynamics of the observer are asymptotically stable. Additionally, the inequality

$$\int_t^\infty z^T(s) Q_o z(s)\, ds < V_o(z_t), \tag{41}$$

holds, where the functional V_o reads as

$$\begin{aligned} V_o(z_t) =& z^T(t)\bar{E}Qz(t) + \int_{t-\tau}^t z^T(s)Hz(s)\, ds \\ &+ \tau \int_{t-\tau}^t \int_\theta^t \dot{z}_1^T(s) M \dot{z}_1(s)\, ds d\theta. \end{aligned} \tag{42}$$

Proof 5. The proof can be found in Appendix E.

Similar to results presented in Theorem 3, (41) functions as a performance measure of the observer. The weighting matrix Q_o can be considered as a parameter by means of which the convergence rate of the state $z(t)$ in (39) can be influenced.

Remark 12. The results in Theorems 3 and 4 are derived by exploiting analysis and controller synthesis technique for delay descriptor systems [32–34].

Summarizing, in this section, we have designed an (observer-based) state-feedback pressure controller for the attenuation of liquid kicks and mud losses for single-phase flow MPD scenarios. This controller has been designed based on the reduced-complexity delay model proposed in Section 3. To implement this controller, only the surface pressure measurements are required. Moreover, degrees of freedom have been provided to enable the heuristic enforcement of a desirable transient control performance. A flow chart of the controller design procedure from the model reduction stage to implementation is presented in Fig. 4. The next section presents illustrative simulation results on realistic drilling scenarios.

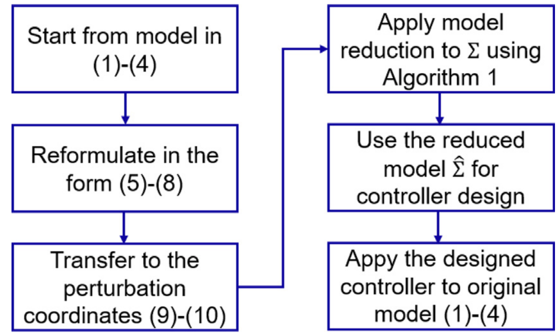

Fig. 4. A flow chart summarizing the design procedure from model reduction to controller implementation.

5. Simulation case studies

In this section, we study the performance of the proposed pressure controller through numerical examples for a drilling system with the parameters listed in Table 1. We first study the accuracy of the reduced-complexity model by comparing it against the original model in the frequency domain. Afterwards, the controller designed on the basis of the reduced delay model of Section 3 is applied to the original model in (9) and (10) to evaluate its performance in comparison to an existing pressure controller from [9] and an intuitive proportional–integral (PI) pressure controller. The former controller has been designed based on a variant of a commonly used, low-complexity model which does not capture the wave propagation effects [8]. This

Table 1
Parameters of the drilling system.

Par.	Value	Unit	Par.	Value	Unit
d_a	0.0953	m	A_a	0.02613	m^2
d_d	0.1088	m	A_d	0.0093	m^2
l	2320	m	θ	1.4455	rad
c_l	980	m/s	k_{res}	6.3×10^{-6}	ms
A_{nz}	5.77×10^{-4}	m^2	c_d	0.8	–
ρ_0	1260	kg/m^3	μ	0.035	Pa s
k_c	0.002	m^2	g	9.81	m/s^2

comparison illustrates advantages of considering the wave propagation effect in the model and controller design procedure for MPD automation.

5.1. Model reduction

In this example, we use the proposed technique in Section 3 to obtain the reduced model $\hat{\Sigma}$ for the considered drilling system dynamics. It is recalled that the input to Σ is v, whereas its output w consists of the perturbed pump density $\tilde{\rho}_p$, downhole density $\tilde{\rho}_{\rm dh}$ and choke density $\tilde{\rho}_c$. Here, the reformulated model Σ in (9) is indeed that of the linearized model around an operating profile that corresponds to $z_c^* = 0.3, J_p^* = 51$ kg/s and $\rho_{\rm res}^* = \rho_{\rm dh}^*$.

To construct the realization of $\Sigma_{\rm ctde}$, we take 6 pairs of complex conjugate interpolation points on the imaginary axis in the frequency interval $|\omega| \in [-0.07\pi/\tau, 2\pi/\tau] + 10^4$, where we can be confident that $T(j\omega)$, the frequency response function of Σ, is almost completely periodic. This leads to $n_2 = 6$. For $\Sigma_{\rm ode}$, by contrast, we select only 4 pairs of complex conjugate interpolations points on the imaginary axis in a low frequency range of $|\omega| \in (0, 1.5]$, leading the order of this subsystem to be $n_1 = 4$. As expected, see Remark 8, all the poles of $\Sigma_{\rm ode}$ are located in the open left-half complex plane and those of $\Sigma_{\rm ctde}$ are located inside the unit circle. This guarantees the exponential stability of the reduced model $\hat{\Sigma}$ for $\hat{v} = 0$.

A comparison between the frequency response function $\hat{T}(j\omega)$ of the reduced system $\hat{\Sigma}$ and that of the original system Σ is reported in Fig. 5. From this figure, a highly accurate model approximation is observed in the high frequency range, while a relatively less accurate approximation is achieved in the lower frequency ranges. To improve the accuracy of the approximation at the lower frequencies, one can increase the order n_1 of $\Sigma_{\rm ode}$. However, we here prefer to settle for a less accurate model in exchange for an approximative model $\hat{\Sigma}$ of a lower order because lower n_1 and n_2 limit the computational burden of solving the matrix inequalities in (32) and (40).

5.2. Closed-loop simulations

Now, let us compare in this section the performance of the observed-based, state-feedback pressure controller presented in Section 4 to the pressure controller presented in [9] and the PI pressure controller. At the start of all simulations in this section, the system is at its steady state. Following this, we take $\hat{x}_0 = 0$ and $\hat{w}(0) = 0$ in all simulations. The reservoir pressure, as a disturbance input, is depicted in Fig. 6. This reservoir pressure resembles the scenarios of suddenly running into a high-pressure zone and into a low-pressure zone. It should be noted that these two scenarios do not necessarily occur successively in practice. The intention here is to study the performance of the controller for a variety of scenarios in a single case study for the sake of brevity. Such a scenario was also considered for the evaluation of pressure controllers in, e.g., [35].

The controller in [9] has been designed on the basis of a simplified second-order model which only consists of the slow pressure dynamics of a drilling system. In this model, the fast dynamics responsible for the wave propagation effects are compromised in exchange for simplicity. This switching pressure controller consists of three observers which estimate the bit flow, the reservoir pressure and the flow exchange between the reservoir and well bore. The control law of [9] in terms of the perturbed choke volumetric flow rate Δq_c [m^3/s] can be written in the following form:

$$\Delta q_c(t) = k_s\sigma(t)\left(\Delta p_{\rm dh}(t) - \Delta\hat{p}_{\rm res}(t)\right) + \hat{q}_{\rm bit}(t), \tag{43}$$

where Δ is used to indicate the variables of this control system in their respective perturbed coordinates. Moreover, k_s is a design parameter and $\hat{p}_{\rm res}$ and $\hat{q}_{\rm bit}$ are the estimated reservoir pressure and the estimated flow exchange between the reservoir and wellbore, respectively. Furthermore, $\sigma(t)$ is a switching variable. The estimated variables and the switching signal are solutions to

$$\begin{aligned}
\Delta\dot{\hat{q}}_{\rm bit}(t) &= -\gamma_1(\Delta p_p(t) - \Delta\hat{p}_p(t)),\\
\Delta\dot{\hat{p}}_p(t) &= \frac{\beta_d}{V_d}\left(\Delta\hat{q}_{\rm bit}(t) + l_1(\Delta p_p(t) - \Delta\hat{p}_p(t))\right),\\
\dot{\hat{q}}_{\rm res}(t) &= \gamma_2(\Delta p_1(t) - \Delta\hat{p}_1(t)),\\
\Delta\dot{\hat{p}}_1(t) &= \hat{q}_{\rm res}(t) - \Delta q_c(t) + l_2(\Delta p_1(t) - \Delta\hat{p}_1(t)),\\
\Delta\dot{\hat{p}}_{\rm res}(t) &= \gamma_3(\Delta p_1(t) - \Delta\hat{p}_2(t)),\\
\Delta\dot{\hat{p}}_2(t) &= \bar{k}_{\rm res}\left(\Delta\hat{p}_{\rm res}(t) - \Delta p_{\rm dh}(t)\right) - \Delta q_c(t)\\
&\quad + l_3\left(\Delta p_1(t) - \Delta\hat{p}_2(t)\right),\\
\sigma(t) &= \begin{cases} 1, & \left|\hat{q}_{\rm res}\right| < \bar{q}_{\rm res},\\ 0, & \text{otherwise.}\end{cases}
\end{aligned} \tag{44}$$

In these dynamics, γ_1, γ_2, γ_3 and l_1, l_2, l_3 are design parameters, whereas $\hat{q}_{\rm res}$ and $\hat{p}_p$ are estimates of the reservoir flow and the pump pressure, respectively. Moreover, p_p is the measured pump pressure and $\Delta p_1 = V_{\rm a}/\beta_{\rm a}\Delta p_c + V_{\rm d}/\beta_{\rm d}\Delta p_p$, with $V_{\rm a}$ and $V_{\rm d}$ being the volume of the annulus and drillstring, respectively. Here, $\beta = c_l^2\rho$ represents the bulk modulus. Finally, $\bar{q}_{\rm res}$ is a threshold parameter for the switching action, and the constant $\bar{k}_{\rm res}$ is an approximation of $k_{\rm res}/\rho_{\rm dh}(t)$. Note that in this controller $\Delta p_{\rm dh} = \Delta p_p$ for a fixed pump flow rate.

Remark 13. To apply the controller (43) to the system, the choke volumetric flow rate Δq_c should be converted to the choke opening $\tilde{z}_c$. To this end, we use the choke equation in (3) to obtain

$$\tilde{z}_c(t) = \frac{\left(\Delta q_c(t) + q_c^*\right)\sqrt{\left(y_{{\rm m},2}(t) + \rho_c^*\right)}}{\sqrt{2\left(y_{{\rm m},2}(t) + \rho_c^* - \rho_0\right)}} - z_c^*.$$

We also consider a PI pressure controller in our comparative studies. This controller is given by [36]

$$\tilde{z}_c(t) = -k_p\left(\tilde{q}_p(t) - \tilde{q}_c(t)\right) - k_i\int_0^t \left(\tilde{q}_p(s) - \tilde{q}_c(s)\right)\, ds, \tag{45}$$

where q_c is the measured choke volumetric flow rate and q_p is that of the pump, and k_i and k_p are the integral and proportional gains of the PI controller. This controller works based on the error between the pump and choke flow rates. Clearly, any error between q_c and q_p (at the same pressures) in the steady state is due to a flux exchange between the reservoir and the wellbore, and regulating this error to zero ensures that the downhole pressure is tracking the reservoir pressure. It is recalled that in this study, we have considered scenarios with a fixed pump flow rate and, subsequently, $\tilde{q}_p = 0$. Nonetheless, it should be noted that even though the structure of the PI controller is quite elementary, the PI controller alone is rarely if ever used in practice because it

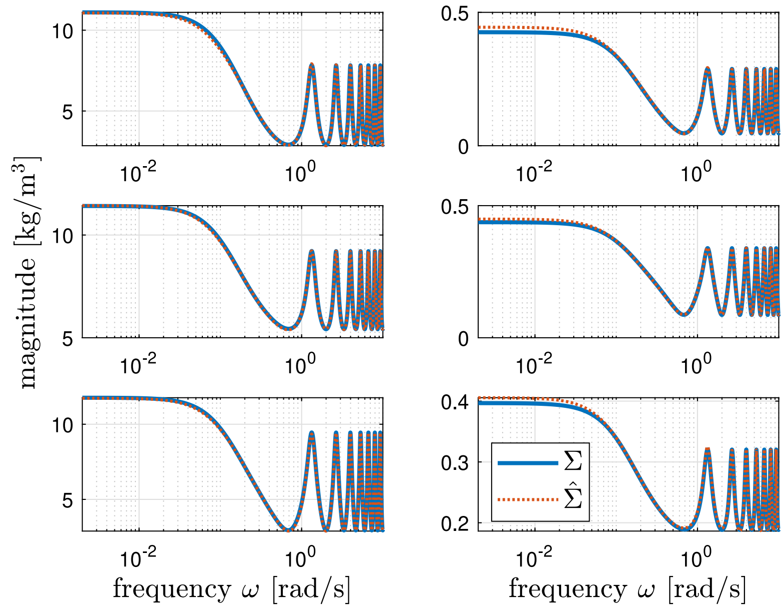

Fig. 5. Comparison between the magnitude of the frequency response function of Σ with that of $\hat{\Sigma}$. The inputs are ψ_1 and ψ_2, and the outputs are the perturbed pump, downhole and choke densities.

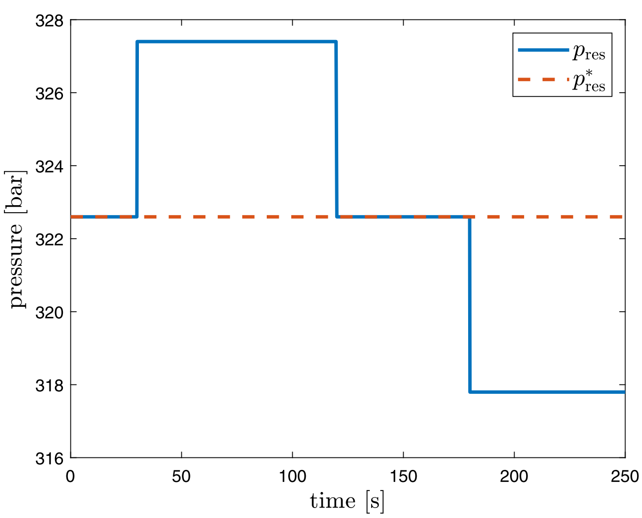

Fig. 6. The reservoir pressure p_{res} considered in the simulations.

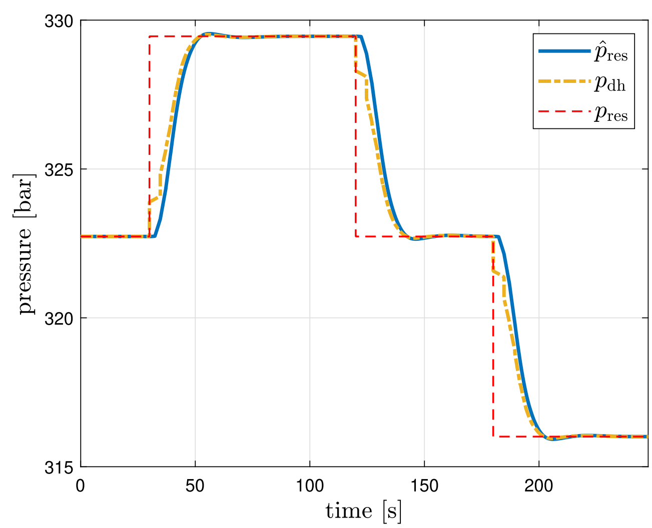

Fig. 7. The time response of the closed-loop system with the proposed controller for the downhole and estimated reservoir pressures applied to $\hat{\Sigma}$.

requires accurate and instantaneous choke flow measurements. Flow measurements are usually not accurate enough in practice for this purpose.

In the first part of the closed-loop simulations, we study the performance of the presented controller by applying it to the reduced delay model $\hat{\Sigma}$, without considering the nonlinearities. After making sure that the performance of the controller is satisfactory in this setting, we apply it to the original nonlinear model described in (9) and (10).

Fig. 7 depicts the estimated reservoir pressure $\hat{p}_{\text{res}}$ in comparison to the downhole pressure p_{dh} response. The corresponding control input z_c is illustrated in Fig. 8. We observe that not only does the downhole pressure track the reservoir pressure with zero steady-state error, but it also exhibits a relatively fast transient response (fast relative to existing results in, e.g., [9]). Fig. 7 also depicts that the estimated reservoir pressure converges to its true value p_{res} with zero steady-state error. In spite of the fact that the reservoir pressure changes abruptly, initiating undesirable sharp propagating pressure waves in the flow path, it is clear from Fig. 7 that the controller effectively attenuates the subsequent fluctuations and provides a smooth downhole pressure response during the transients. We attribute this desirable performance of the controller to the fact that it has been designed based on a model in which the wave propagation effects have been preserved. A comparison between the (perturbed) pump, downhole and choke pressure is reported in Fig. 9. One can observe from this figure that the wave propagation-induced pressure fluctuations have been attenuated also in the pump and choke pressure signals.

Remark 14. We note that such fluctuations are undesirable because those are detrimental to the drilling equipment and the reservoir productivity. In particular, those can intensify wear and tear in the drilling equipment such as the sensors installed in the bottom-hole assembly and the choke manifold.

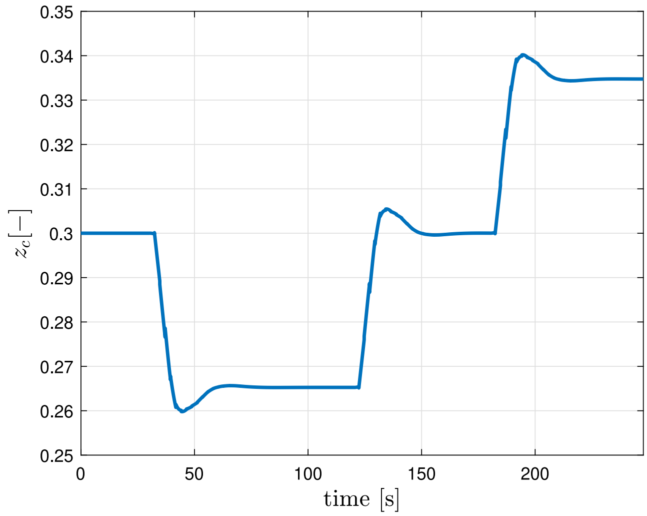

Fig. 8. The choke opening for the closed-loop system with the reduced model $\hat{\Sigma}$ and the proposed controller .

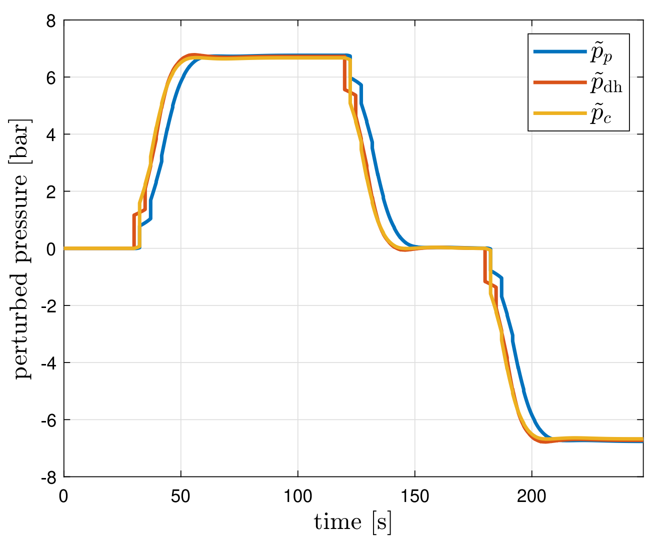

Fig. 9. The time response of the closed-loop system with $\hat{\Sigma}$ and the proposed controller for the perturbed pump, downhole and choke pressures.

Table 2
Parameters used in the PI controller and the controller from [9].

Parameter	Value	Parameter	Value
l_1	7.3×10^{-7}	γ_1	0.075
l_2	0.61	γ_2	0.093×10^{-4}
l_3	0.57	γ_3	1.24×10^{7}
k_s	1.3×10^{-3}	$\bar{q}_{\rm res}$	0.5 [lit/s]
k_i	1	k_p	1.3×10^{-3}

Next, we apply the proposed controller to the original nonlinear PDE model in (9) and (10), expecting to observe a closed-loop response similar to what we have observed for $\hat{\Sigma}$ in the previous part. We should expect this similarity because of the good accuracy of the approximate model. To implement the PDE model, we have discretized it using a staggered-grid discretization scheme, see, e.g., [37]. At the same time, we also apply the controllers in (43) and (45) to Σ for the sake of a comparative study. The parameters of these two controllers are listed in Table 2.

We have reported the downhole pressure response $p_{\rm dh}$ in Fig. 10. From this figure, we can clearly deduce that in terms of

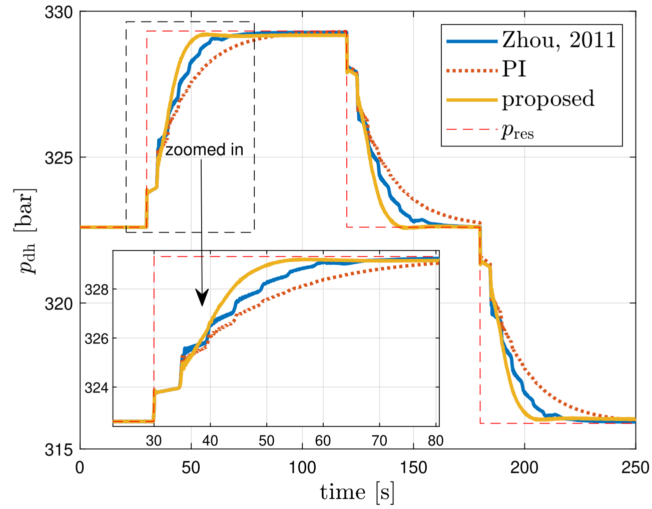

Fig. 10. Comparison in terms of the downhole pressure response between the performance of the proposed controller, PI controller and that from [9] applied to the original nonlinear model.

transient response, the proposed controller outperforms the other two controllers, whereas all controllers provide similar steady-state performance. In particular, the proposed controller has a faster response in terms of the downhole pressure tracking the reservoir pressure. A faster downhole pressure response is an advantage because it reduces the size of kicks and mud losses. Moreover, for the PI controller and the controller from [9], we can clearly observe undesirable wave propagation-induced fluctuations in the downhole pressure, while the pressure response with the proposed controller is smoother. Indeed, not only are these controllers incapable of attenuating these fluctuations, but the resulting closed-loop system can also not be guaranteed to maintain its stability in the presence of these fluctuations. Fig. 11 shows the choke opening signals for these three controllers. As anticipated, we observe that the proposed controller has a faster control action. The closed-loop responses for the choke and pump pressures are depicted in Fig. 12. As expected, we can also observe severe fluctuations in these pressure signals for the controllers from the literature.

Remark 15. We mention that, in real-life drilling systems, special pressure dampers are usually installed at the pump side of the flow path to passively damp such pressure fluctuations and protect the rig pumps from the resulting impacts. Clearly, the possibility to damp such fluctuations in an active way by means of a control system can have benefits such as lowering construction and maintenance costs of a drilling rig.

6. Conclusions

In this paper, a data-based model reduction technique has been presented for control-oriented modeling for managed pressure drilling automation in single-phase flow scenarios. The new structure proposed for the reduced model consists of a system of continuous-time difference equations and a system of ordinary differential equations. The former part is in a class of time delay systems and it is responsible for accurately capturing the wave propagation effect of the original PDE-based hydraulics model, while the latter part of the reduced model ensures approximation of the slow hydraulics in a drilling system. In view of its high accuracy, yet low complexity, the reduced-complexity model has

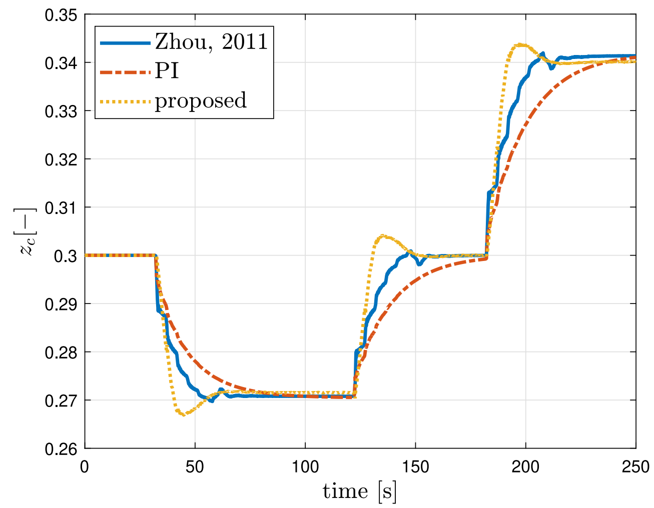

Fig. 11. The choke opening signal z_c for the proposed controller, PI controller and that from Zhou, 2011 [9] applied to the original nonlinear model.

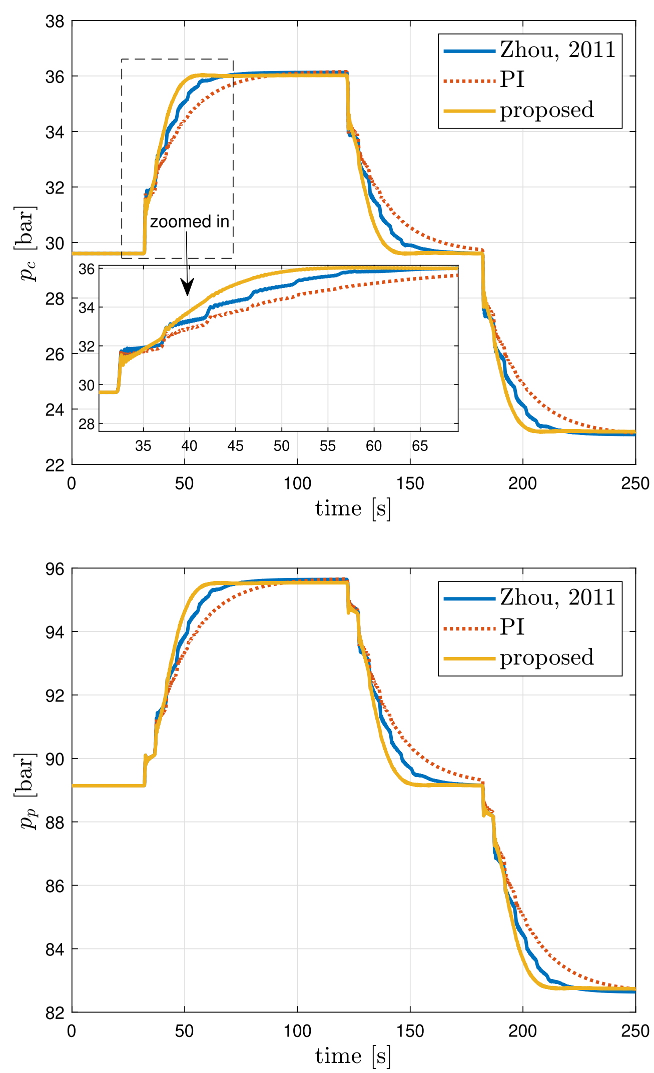

Fig. 12. Comparison in terms of the choke and pump pressure responses between the performance of the proposed controller, the PI controller and that from Zhou, 2011 [9] applied to the original nonlinear model.

been used to design a new pressure control system for preventing/attenuating liquid kicks and mud losses. Results on synthesis conditions for stability and performance have been presented. This controller, which only requires the surface pressure measurements, has been compared to existing pressure controllers designed based on a model that does not capture the wave propagation effect. By means of simulation studies, it has been shown that the proposed controller outperforms existing controllers in terms of the rise time for the downhole pressure, which leads to smaller kicks and losses, and attenuation of undesirable pressure fluctuations due to the wave propagation effects.

Declaration of competing interest

The authors declare that they have no known competing financial interests or personal relationships that could have appeared to influence the work reported in this paper.

Data availability

Data will be made available on request.

Acknowledgments

This research has been carried out in the HYDRA project, which has received funding from the European Union's Horizon 2020 research and innovation program under grant agreement No 675731.

Appendix A. Reformulation of the boundary conditions

We would like to transform the boundary conditions in (3) to the perturbation coordinates and rewrite them in the form (7). It is recalled that the origin of the new coordinates is the system steady-state solution ρ_i^* and η_i^*, $i = \mathrm{a}, \mathrm{d}$, that corresponds to the nominal inputs J_p^*, z_c^* and ρ_{res}^*. In the perturbation coordinates, the first equation in (3) can be written as

$$A_{\mathrm{d}}\tilde{\eta}_{\mathrm{d}}(t,l) + T_{15}\tilde{\rho}_{\mathrm{d}}(t,l) + T_{13}\tilde{\rho}_{\mathrm{dh}}(t) + h_1\left(\tilde{\rho}_{\mathrm{d}}(t,l), \tilde{\rho}_{\mathrm{dh}}(t)\right) = 0,$$

where it is recalled that $\tilde{\eta}_{\mathrm{d}} = \eta_{\mathrm{d}} - \eta_{\mathrm{d}}^*$, $\tilde{\rho}_{\mathrm{d}} = \rho_{\mathrm{d}} - \rho_{\mathrm{d}}^*$ and $\tilde{\rho}_{\mathrm{dh}} = \rho_{\mathrm{dh}} - \rho_{\mathrm{dh}}^*$. Moreover, the nonlinearity in that equation has been split into a linear part and a nonlinear part $h_1(\cdot,\cdot)$. The linear part is obtained by linearizing the nonlinear terms around the steady-state solution, leading to

$$T_{13} = \frac{A_{\mathrm{nz}}c_d c_l \rho_{\mathrm{d}}^*(l)}{\sqrt{2\rho_{\mathrm{d}}^*(l)\left(\rho_{\mathrm{d}}^*(l) - \rho_{\mathrm{dh}}^*\right)}}, \; T_{15} = \frac{-A_{\mathrm{nz}}c_d c_l\left(2\rho_{\mathrm{d}}^*(l) - \rho_{\mathrm{dh}}^*\right)}{\sqrt{2\rho_{\mathrm{d}}^*(l)\left(\rho_{\mathrm{d}}^*(l) - \rho_{\mathrm{dh}}^*\right)}}.$$

Similarly, the third boundary condition in (3) can be written in the perturbation coordinates as follows:

$$T_{38}\tilde{\eta}_{\mathrm{a}}(t,l) + T_{37}\tilde{\rho}_c(t) - \tilde{z}_c(t) - h_2\left(\tilde{\rho}_c(t), \tilde{z}_c(t)\right) = 0,$$

where $\tilde{\eta}_{\mathrm{a}} = \eta_{\mathrm{a}} - \eta_{\mathrm{a}}^*$, $\tilde{\rho}_c = \rho_c - \rho_c^*$ and $\tilde{z}_c = z_c - z_c^*$, and the constants T_{38} and T_{37} and the nonlinear term h_2 are given by

$$\begin{aligned} T_{37} &= \frac{-z_c^*\left(2\rho_c^* - \rho_0\right)}{2\rho_c^*\left(\rho_c^* - \rho_0\right)}, \quad T_{38} = \frac{A_{\mathrm{a}}}{k_c c_l\sqrt{2\rho_c^*\left(\rho_c^* - \rho_0\right)}}, \\ h_2 &= T_{37}\rho_c(t) + \tilde{z}_c - z_c^* + \frac{z_c\sqrt{2\rho_c(t)\left(\rho_c(t) - \rho_0\right)}}{\sqrt{2\rho_c^*\left(\rho_c^* - \rho_0\right)}}. \end{aligned} \tag{46}$$

This finally leads to the formulation of the boundary conditions in perturbation coordinates as in (7) with the matrix Π_1 given by

$$\Pi_1 = \begin{bmatrix} 0 & 0 & T_{13} & 0 & T_{15} & 0 & 0 & 0 \\ 0 & 0 & -k_r c_l^2 & -A_{\mathrm{a}} & 0 & A_{\mathrm{d}} & 0 & 0 \\ 0 & 0 & 0 & 0 & 0 & 0 & T_{37} & T_{38} \\ 0 & A_{\mathrm{d}} & 0 & 0 & 0 & 0 & 0 & 0 \end{bmatrix}. \tag{47}$$

The function ψ is thus defined as $\psi := [\tilde{z}_c + h_2, \tilde{\rho}_{\mathrm{res}}, h_1]^T$. Considering the order of the boundary conditions in (3) and the definition of ψ, we obtain

$$\Pi_2 = \begin{bmatrix} 0 & 0 & 1 \\ 0 & -k_{\mathrm{res}}c_l^2 & 0 \\ 1 & 0 & 0 \\ 0 & 0 & 0 \end{bmatrix}. \tag{48}$$

The first argument of the function $\psi(\cdot,\cdot)$ is the vector $[q_{d,1}(t,l), \tilde{\rho}_{\mathrm{dh}}(t), \tilde{\rho}_c(t)]^T$, which should be extracted from $[Q^T(t,0), Q^T(t,l)]^T$ by Γ. Following the definition of Q in (5), we thus obtain

$$\Gamma = \begin{bmatrix} 1 & 0 & 0 & 0 & 0 & 0 & 0 & 0 \\ 0 & 0 & 1 & 0 & 0 & 0 & 0 & 0 \\ 0 & 0 & 0 & 0 & 0 & 0 & 1 & 0 \end{bmatrix}. \tag{49}$$

Appendix B. Proof of Lemma 1

By applying a Laplace transformation to the PDE in (9), we obtain

$$sQ(s,\xi) + \Psi_c \frac{\partial}{\partial \xi} Q(s,\xi) + F_c Q(s,\xi) = 0, \tag{50}$$

where $Q(s,\xi) = \mathcal{L}(Q(t,\xi))$, with $\mathcal{L}(\cdot)$ the Laplace operator. This equation can also be written in the form

$$\frac{\partial}{\partial \xi} Q(s,\xi) = \Xi(s) Q(s,\xi), \tag{51}$$

with $\Xi(s) = -\Psi_c^{-1}(sI_4 + F_c)$. Note that for fixed s, (51) is a linear, ordinary differential equation with the independent variable ξ. Thus, its general solution is given by

$$Q(s,\xi) = e^{\Xi(s)\xi} X(s), \tag{52}$$

where $X(s)$ is obtained from the boundary conditions. Specifically, the evaluation of (52) for $\xi = 0$ and $\xi = l$ together with the use of the boundary conditions in (9) results in

$$\Pi_1 \begin{bmatrix} e^{\Xi(s)0} \\ e^{\Xi(s)l} \end{bmatrix} X(s) = \Pi_2 V(s),$$

where $V(s) = \mathcal{L}(v(t))$. Solving this equation leads to

$$X(s) = \left(\Pi_1 \begin{bmatrix} I_4 \\ e^{\Xi(s)l} \end{bmatrix} \right)^{-1} \Pi_2 V(s).$$

Now, the use of this result, along with (52), in the output equation in (9) yields (11).

Appendix C. Periodicity of $\exp(\Xi_i(s)\xi)$

In this section, we provide an argument for the fact that $\exp(\Xi_i(j\omega)\xi)$ in Lemma 1 converges to a periodic behavior at high frequencies. Here, we show this fact only for the upper-left element of this matrix, that is, we show that $m_{11}(j\omega,\xi)$ in (13) converges to a periodic function for $\omega \to \infty$. To this end, we first rewrite $\beta(j\omega)$, defined below (14), as

$$\beta(j\omega) = \frac{|\omega|\sqrt{\left(c^2\alpha^2 + f_{11}f_{22} - f_{12}f_{21} - 1\right) + j\frac{f_{11}+f_{22}}{\omega}}}{c_l}.$$

For this expression, we obtain

$$\lim_{\omega\to\infty} \beta(j\omega) = \frac{1}{c_l}|\omega| e^{j\left(\frac{\pi}{2} - \frac{f_{11}+f_{22}}{2\omega}\right)}.$$

Now, using Euler's formula, this limit can further be simplified as

$$\lim_{\omega\to+\infty} \beta(j\omega) = \frac{1}{c_l}\left(j\omega + \frac{f_{11}+f_{22}}{2}\right). \tag{53}$$

This clearly implies that $\lim_{\omega\to\infty}|\beta| = \infty$. Therefore, we can ignore the second term on the right-hand side of (13) in the limit of $\omega \to +\infty$ and write

$$\lim_{\omega\to+\infty} m_{11}(j\omega,\xi) = \cosh\left(\frac{\xi}{c_l}\left(j\omega + \frac{f_{11}+f_{22}}{2}\right)\right), \tag{54}$$

where (53) has been substituted in (13). This limit can further be written in the following form:

$$\lim_{\omega\to+\infty} m_{11}(j\omega,\xi) = \cosh\left(\frac{\xi}{c_l}\frac{f_{11}+f_{22}}{2}\right)\cos\left(\frac{\xi}{c_l}\omega\right) + j\sinh\left(\frac{\xi}{c_l}\frac{f_{11}+f_{22}}{2}\right)\sin\left(\frac{\xi}{c_l}\omega\right).$$

The function on the right-hand side of this equality is clearly a periodic function of ω with a period of $2\pi c_l/\xi$. A similar argument can be used to show that all other elements of $\exp(\Xi_i\xi)$ are periodic functions with the same period.

Appendix D. Proof of Theorem 3

To prove this theorem, we first need to show that the delay-difference part of the system (31), i.e., $0 = A_{c,22}\tilde{x}_2(t) + A_{\mathrm{d},22}\tilde{x}_2(t-\tau)$ with $A_{c,22}, A_{\mathrm{d},22}$ respectively the lower-right $n_2 \times n_2$ blocks of A_c, A_{d}, is asymptotically stable. The satisfaction of (32) for a nonsingular P_3 implies that $\Phi_{11} < 0$, which in turn implies

$$A_{c,22}P_3 + P_3^T A_{c,22}^T + U_{22} < 0, \tag{55}$$

with U_{22} being the lower-right $n_2 \times n_2$ block of U. Since $U_{22} > 0$ and P_3 is full-rank, (55) implies that $A_{c,22}$ is non–singular. The satisfaction of (32) also implies that

$$\begin{bmatrix} A_{c,22}^T P_3^{-1} + P_3^{-T} A_{c,22} + \bar{U}_{22} & P_3^{-T} A_{\mathrm{d},22} \\ A_{\mathrm{d},22}^T P_3^{-1} & -\bar{U}_{22} \end{bmatrix} < 0,$$

with $\bar{U}_{22}$ the lower-right $n_2 \times n_2$ blocks of $\bar{U}$. This result further implies that

$$A_{c,22}^T P_3^{-1} + P_3^{-T} A_{c,22} + \bar{U}_{22} + P_3^{-T} A_{\mathrm{d},22} \bar{U}_{22}^{-1} A_{\mathrm{d},22}^T P_3^{-1} < 0,$$

where a Schur complement has been used. Multiplying this inequality from the right by a non-zero vector $v \in \mathbb{C}^{n_2}$ and from the left by its conjugate transpose v^H, we obtain

$$-2\left|v^H A_{c,22}^T P_3^{-1} v\right| + \left|\bar{U}_{22}^{1/2} v\right|^2 + \left|\bar{U}_{22}^{-1/2} A_{\mathrm{d},22}^T A_{c,22}^{-T} A_{c,22}^T P_3^{-1} v\right|^2 < 0.$$

Thus, it holds that

$$-\left|v^H A_{c,22}^T P_3^{-1} v\right| + \left|v^H A_{\mathrm{d},22}^T A_{c,22}^{-T} A_{c,22}^T P_3^{-1} v\right| < 0, \tag{56}$$

where the inequality

$$\left|\bar{U}_{22}^{1/2} v\right|^2 + \left|\bar{U}_{22}^{-1/2} A_{\mathrm{d},22}^T A_{c,22}^{-T} A_{c,22}^T P_3^{-1} v\right|^2 \geq 2\left|v^H A_{\mathrm{d},22}^T A_{c,22}^{-T} A_{c,22}^T P_3^{-1} v\right|,$$

has been used. Now, if we take v to be any eigenvector of $A_{c,22}^{-1} A_{\mathrm{d},22}$ with the corresponding eigenvalue $\lambda = \lambda(A_{c,22}^{-1} A_{\mathrm{d},22})$, then (56) implies that

$$-\left|v^H A_{c,22}^T P_3^{-1} v\right| + |\lambda|\left|v^H A_{c,22}^T P_3^{-1} v\right| < 0,$$

which implies that $|\lambda| < 1$, meaning that the delay-difference part of the system (31) is asymptotically stable.

Next, we consider the functional in (34) as a candidate Lyapunov–Krasovskii functional. For the time derivative of the

$$\begin{bmatrix} A^T\bar{P}+\bar{P}^TA+\bar{U}-\alpha_c\Lambda^T\bar{P}_1\Lambda-K_{\rm sf}^TB^T\bar{P}-\bar{P}^TBK_{\rm sf}+Q_h^TQ_h+\gamma^2K_{\rm sf}^TK_{\rm sf} & * & * \\ A_{\rm d}^T\bar{P}+\alpha_c\Lambda^T\bar{P}_1\Lambda & -\bar{U}-\alpha_c\Lambda^T\bar{P}_1\Lambda & * \\ \tau\bar{P}_1\Lambda\,(A-BK_{\rm sf}) & \tau\bar{P}_1\Lambda A_{\rm d} & \alpha_c^{-1}\bar{P}_1 \end{bmatrix} < 0. \tag{60}$$

Box I.

Lyapunov–Krasovskii functional (34) along the solution of (31), we obtain

$$\begin{aligned}\dot{V}_c(\tilde{x}_t) = {} & 2\left(A_c\tilde{x}(t)+A_{\rm d}\tilde{x}(t-\tau)\right)^T\bar{P}\tilde{x}(t)\\ & +\tilde{x}^T(t)\bar{U}\tilde{x}(t)-\tilde{x}^T(t-\tau)\bar{U}\tilde{x}(t-\tau)\\ & +\alpha_c\tau^2\dot{\tilde{x}}_1^T(t)\bar{P}_1\dot{\tilde{x}}_1(t)-\alpha_c\tau\int_{t-\tau}^{t}\dot{\tilde{x}}_1^T(s)\bar{P}_1\dot{\tilde{x}}_1(s)ds.\end{aligned}$$

Given the fact that $\dot{\tilde{x}}_1(t)=\Lambda E\dot{\tilde{x}}(t)$, we can write the above in the following form:

$$\begin{aligned}\dot{V}_c(\tilde{x}_t) = {} & 2(A_c\tilde{x}(t)+A_{\rm d}\tilde{x}(t-\tau))^T\bar{P}\tilde{x}(t)\\ & +\tilde{x}^T(t)\bar{U}\tilde{x}(t)-\tilde{x}^T(t-\tau)\bar{U}\tilde{x}(t-\tau)\\ & +\alpha_c\tau^2\dot{\tilde{x}}^T(t)E^T\Lambda^T\bar{P}_1\Lambda E\dot{\tilde{x}}(t)\\ & -\alpha_c\tau\int_{t-\tau}^{t}\dot{\tilde{x}}_1^T(s)\bar{P}_1\dot{\tilde{x}}_1(s)ds.\end{aligned} \tag{57}$$

Applying Jensen's inequality [38] to the last term in the right-hand side of (57), we further obtain

$$\begin{aligned}\dot{V}_c(\tilde{x}_t) \le {} & 2(A_c\tilde{x}(t)+A_{\rm d}\tilde{x}(t-\tau))^T\bar{P}\tilde{x}(t)\\ & +\tilde{x}^T(t)\bar{U}\tilde{x}(t)-\tilde{x}^T(t-\tau)\bar{U}\tilde{x}(t-\tau)\\ & +\alpha_c\tau^2\dot{\tilde{x}}^T(t)E^T\Lambda^T\bar{P}_1\Lambda E\dot{\tilde{x}}(t)\\ & -\alpha_c\left(\tilde{x}(t)-\tilde{x}(t-\tau)\right)^T\Lambda^T\bar{P}_1\Lambda\left(\tilde{x}(t)-\tilde{x}(t-\tau)\right).\end{aligned}$$

where $\tilde{x}_1=\Lambda\tilde{x}$ has been used. Substituting (31) into this inequality leads to

$$\dot{V}_c(\tilde{x}_t)\le\zeta_c^T(t)\left(M_c+\alpha_c\tau^2G^T\Lambda^T\bar{P}_1\Lambda G\right)\zeta_c(t), \tag{58}$$

with $\zeta_c^T(t)=[\tilde{x}^T(t),\tilde{x}^T(t-\tau)]$ and $G=[A_c,A_{\rm d}]$ and some matrix M_c.

Clearly, if

$$\dot{V}_c(\tilde{x}_t)+\tilde{x}^T(t)Q_h^TQ_h\tilde{x}(t)+\gamma^2\tilde{x}^T(t)K_{\rm sf}^TK_{\rm sf}\tilde{x}(t)<0, \tag{59}$$

holds, given the fact that $|\lambda(A_{c,22}^{-1}A_{\rm d,22})|<1$ also holds, it is guaranteed that (31) is asymptotically stable due to the Lyapunov–Krasovskii stability theorems [34]. Note that always $Q_h^TQ_h+\gamma^2K_{\rm sf}^TK_{\rm sf}\ge 0$. We can show that the satisfaction of the matrix inequity (60) (see Box I), guarantees the satisfaction of the inequality (59). Applying Schur complements to (32), and then left and right multiplication of the resulting inequality with blkdiag$\{\bar{P}^T,\bar{P}^T,\bar{P}_1^T\}$ and blkdiag$\{\bar{P},\bar{P},\bar{P}_1\}$, reveals that (32) implies (60). Therefore, the satisfaction of (32) implies the asymptotic stability of (31). This completes the first part of the proof.

Next, we prove the validity of the inequality in (33). Integrating the inequality (59) over $[t,\infty)$ yields

$$\left(\lim_{t\to\infty}V_c(\tilde{x}_t)\right)-V_c(\tilde{x}_t)+\int_t^\infty\left(\tilde{x}^T(s)Q_h^TQ_h\tilde{x}(s)+\gamma^2u_{\rm sf}^2(s)\right)ds<0.$$

The asymptotic stability of (31) implies that $V_c(\tilde{x}_\infty)=0$. Thus, (33) follows.

Appendix E. Proof of Theorem 4

We first need to show that the delay-difference part of the error dynamics in (39), i.e., $0=\bar{A}_{o,22}z_2(t)+\bar{A}_{\rm d,22}z_2(t-\tau)$, is asymptotically stable. Here, $\bar{A}_{o,22}$ and $\bar{A}_{\rm d,22}$ are the lower-right $n_2\times n_2$ blocks of $\bar{A}_o:=\bar{A}-L\bar{C}$ and $\bar{A}_{\rm d}$, respectively, and $z_2=x_2-\hat{x}_2$ is the lower part of z that corresponds to these matrices. To this end, we first eliminate the variables S and α_o from the inequality (40) by multiplying it from the left and right by

$$\begin{bmatrix} I & 0 & \bar{A}_o^T \\ 0 & I & \bar{A}_{\rm d}^T\end{bmatrix},\text{ and }\begin{bmatrix} I & 0 & \bar{A}_o^T \\ 0 & I & \bar{A}_{\rm d}^T\end{bmatrix}^T,$$

respectively. Performing this multiplication and then applying a Schur complement reveals that the satisfaction of (40) implies that the following inequality holds:

$$\begin{bmatrix} \bar{A}_o^TQ+Q^T\bar{A}_o+H-\bar{M}+Q_o & * & * \\ \bar{A}_{\rm d}^TQ+\bar{M} & -H-\bar{M} & * \\ \tau M\bar{\Lambda}\bar{A}_o & \tau M\bar{\Lambda}\bar{A}_{\rm d} & -M\end{bmatrix}<0. \tag{61}$$

Now, by following a similar procedure as in the proof of Theorem 3 in Appendix C, (61) can be used to prove that $\bar{A}_{o,22}$ is non-singular. Moreover, it can be proved that all eigenvalues of $\bar{A}_{o,22}^{-1}\bar{A}_{\rm d,22}$ are located within the unit circle, which implies the asymptotic stability of the delay-difference part of the error dynamics.

Next, following a procedure similar to the second part of the proof of Theorem 3, we can show that

$$\begin{aligned}\dot{V}_o(z_t)\le {} & 2\dot{z}^T(t)\bar{E}^TQz(t)+z(t)Hz(t)-z(t-\tau)Hz(t-\tau)\\ & +\tau^2\dot{z}^T(t)\bar{E}^T\Lambda^TM\Lambda\bar{E}\dot{z}(t)\\ & -(z(t)-z(t-\tau))\,\Lambda^TM\Lambda\,(z(t)-z(t-\tau)).\end{aligned}$$

Using the fact that $(\bar{A}-L\bar{C})z(t)+\bar{A}_{\rm d}z(t-\tau)-\bar{E}\dot{z}(t)=0$, we can write this inequality in the following form:

$$\begin{aligned}\dot{V}_o(z_t)\le {} & 2\dot{z}^T(t)\bar{E}^TQz(t)+z(t)Hz(t)-z(t-\tau)Hz(t-\tau)\\ & +\tau^2\dot{z}^T(t)\bar{E}^T\Lambda^TM\Lambda\bar{E}\dot{z}(t)\\ & -(z(t)-z(t-\tau))\,\Lambda^TM\Lambda\,(z(t)-z(t-\tau))\\ & +2\left(z(t)+\alpha_o\bar{E}\dot{z}(t)\right)^TS\left((\bar{A}-L\bar{C})z(t)\right.\\ & \left.+\bar{A}_dz(t-\tau)-\bar{E}\dot{z}(t)\right),\end{aligned}$$

where the last term on the right-hand side is always zero. Now, we add the term $z^T(t)Q_oz(t)$ to both sides of this inequality and obtain

$$\dot{V}_o(z_t)+z^T(t)Q_oz(t)\le\zeta_o^T(t)N\zeta_o(t), \tag{62}$$

where N is the matrix on the left-hand side of (40) with $\bar{L}:=SL$. Given results on the stability of time delay systems, $\dot{V}_o(z_t)<0$, along with the fact the delay-difference part of the error dynamics is asymptotically stable, grantees the asymptotic stability of the error dynamics of the observer. Clearly, the satisfaction of the inequality (40) implies that $N<0$ which guarantees $\dot{V}_o(z_t)<0$, thereby the asymptotic stability of the error dynamics. Now, integrating both sides of (62) over the interval $[t,\infty)$ reveals that

$$\lim_{t\to\infty}V_o(z_t)-V_o(z_t)+\int_t^\infty z^T(s)Q_oz(s)\,ds\le 0.$$

Due to the asymptotic stability of the error dynamics, we have $\lim_{t\to\infty} V_o(z_t) = 0$. This leads to (41) and completes the proof.

References

[1] M.M. Habib, S. Imtiaz, F. Khan, S. Ahmed, J. Baker, Early detection and estimation of kick in managed pressure drilling, SPE Drill. Complet. 36 (02) (2021) 245–262.

[2] J. Beyer, H.C. Trannum, T. Bakke, P.V. Hodson, T.K. Collier, Environmental effects of the Deepwater Horizon oil spill: A review, Mar. Pollut. Bull. 110 (1) (2016) 28–51.

[3] P. Holand, Offshore Blowouts: Causes and Control, Gulf publishing company, Houston, USA, 1997.

[4] G.C. Downton, Challenges of modeling drilling systems for the purposes of automation and control, IFAC Proc. Vol. 45 (8) (2012) 201–210.

[5] B. Rehm, J. Schubert, A. Haghshenas, A.S. Paknejad, J. Hughes, Managed Pressure Drilling, first ed., Gulf Publishing Company, Houston, TX 77046, USA, 2008.

[6] E.J. van Riet, D. Reitsma, B. Vandecraen, Development and testing of a fully automated system to accurately control downhole pressure during drilling operations, in: SPE/IADC Middle East Drilling Technology Conference and Exhibition, Society of Petroleum Engineers, Abu Dhabi, United Arab Emirates, 2003.

[7] M.V. Faronov, I.G. Polushin, Observer-based control of vertical penetration rate in rotary drilling systems, J. Process Control 106 (2021) 29–43.

[8] G.-O. Kaasa, Ø.N. Stamnes, O.M. Aamo, L.S. Imsland, Simplified hydraulics model used for intelligent estimation of downhole pressure for a managed-pressure-drilling control system, SPE Drill. Complet. 27 (01) (2012) 127–138.

[9] J. Zhou, Ø.N. Stamnes, O.M. Aamo, G.O. Kaasa, Switched control for pressure regulation and kick attenuation in a managed pressure drilling system, IEEE Trans. Control Syst. Technol. 19 (2) (2011) 337–350.

[10] I.S. Landet, A. Pavlov, O.M. Aamo, Modeling and control of heave-induced pressure fluctuations in managed pressure drilling, IEEE Trans. Control Syst. Technol. 21 (4) (2013) 1340–1351.

[11] P. Skalle, T. Toverud, S.T. Johansen, Attenuation of pump pressure in long wellbores (v02), J. Pet. Sci. Eng. 122 (2014) 159–165.

[12] S. Naderi Lordejani, B. Besselink, M.H. Abbasi, G.O. Kaasa, W.H.A. Schilders, N. van de Wouw, Control-oriented modeling for managed pressure drilling automation using model order reduction, IEEE Trans. Control Syst. Technol. (2020) 1–14.

[13] A. Albert, O.M. Aamo, J. Godhavn, A. Pavlov, Suppressing pressure oscillations in offshore drilling: Control design and experimental results, IEEE Trans. Control Syst. Technol. 23 (2) (2015) 813–819.

[14] G. Nygaard, G. Nævdal, Nonlinear model predictive control scheme for stabilizing annulus pressure during oil well drilling, J. Process Control 16 (7) (2006) 719–732.

[15] E. Hauge, O.M. Aamo, J.M. Godhavn, G. Nygaard, A novel model-based scheme for kick and loss mitigation during drilling, J. Process Control 23 (4) (2013) 463–472.

[16] A. Nikoofard, U.J.F. Aarsnes, T.A. Johansen, G. Kaasa, State and parameter estimation of a drift-flux model for underbalanced drilling operations, IEEE Trans. Control Syst. Technol. 25 (6) (2017) 2000–2009.

[17] H. Mahdianfar, A. Pavlov, Adaptive output regulation for offshore managed pressure drilling, Internat. J. Adapt. Control Signal Process. 31 (4) (2017) 652–673.

[18] I.S. Landet, H. Mahdianfar, A. Pavlov, O.M. Aamo, Modeling for MPD operations with experimental validation, in: IADC/SPE Drilling Conference and Exhibition, Society of Petroleum Engineers, California, 2012.

[19] M.H. Abbasi, L. Iapichino, S. Naderi Lordejani, W. Schilders, N. van de Wouw, Reduced basis method for managed pressure drilling based on a model with local nonlinearities, Internat. J. Numer. Methods Engrg. Special issue article (2020).

[20] T.C.P.F. Leenen, S. Naderi Lordejani, B. Besselink, W.H.A. Schilders, N. van de Wouw, Control-oriented model reduction for a class of hyperbolic systems with application to managed pressure drilling, in: 21st IFAC World Congress, Berlin, Germany, 2020.

[21] K.L. Cooke, D.W. Krumme, Differential-difference equations and nonlinear initial-boundary value problems for linear hyperbolic partial differential equations, J. Math. Anal. Appl. 24 (2) (1968) 372–387.

[22] E. Kreyszig, Advanced Engineering Mathematics, tenth ed., Wiley, USA, 2011.

[23] M.A. Davó, D. Bresch-Pietri, C. Prieur, F. Di Meglio, Stability analysis of a 2×2 linear hyperbolic system with a sampled-data controller via backstepping method and looped-functionals, IEEE Trans. Automat. Control 64 (4) (2019) 1718–1725.

[24] H. Mahdianfar, O. Morten Aamo, A. Pavlov, Suppression of heave-induced pressure fluctuations in MPD, IFAC Proc. Vol. 45 (8) (2012) 239–244.

[25] U.J.F. Aarsnes, O.M. Aamo, A. Pavlov, Quantifying error introduced by finite order discretization of a hydraulic well model, in: 2nd Australian Control Conference, Sydney, NSW, Australia, 2012, pp. 54–59.

[26] T. Strecker, O.M. Aamo, H. Manum, Simulation of heave-induced pressure oscillations in Herschel-Bulkley muds, SPE J. 22 (05) (2017) 1635–1653.

[27] S. Naderi Lordejani, M.H. Abbasi, N. Velmurugan, C. Berg, J.Å. Stakvik, B. Besselink, L. Iapichino, F. Di Meglio, W.H.A. Schilders, N. van de Wouw, Modeling and numerical implementation of managed-pressure-drilling systems for the assessment of pressure-control systems, SPE Drill. Complet. (2020).

[28] M.H. Abbasi, H. Bansal, H. Zwart, L. Iapichino, W.H.A. Schilders, N. van de Wouw, Power-preserving interconnection of single- and two-phase flow models for managed pressure drilling, in: 2020 American Control Conference, ACC, Denver, USA, 2020, pp. 3097–3102.

[29] U.J.F. Aarsnes, F. Di Meglio, R. Graham, O.M. Aamo, et al., A methodology for classifying operating regimes in underbalanced-drilling operations, SPE J. 21 (02) (2016) 423–433.

[30] P. Schulze, B. Unger, C. Beattie, S. Gugercin, Data-driven structured realization, Linear Algebra Appl. 537 (2018) 250–286.

[31] P. Schulze, B. Unger, Data-driven interpolation of dynamical systems with delay, Systems Control Lett. 97 (2016) 125–131.

[32] E. Fridman, Stability of linear descriptor systems with delay: A Lyapunov-based approach, J. Math. Anal. Appl. 273 (1) (2002) 24–44.

[33] V. Răsvan, S.-I. Niculescu, Oscillations in lossless propagation models: A Liapunov-Krasovskii approach, IMA J. Math. Control Inform. 19 (2002) 157–172.

[34] E. Fridman, Introduction to Time-Delay Systems: Analysis and Control, Birkhauser Boston, 2014.

[35] H. Holta, H. Anfinsen, O.M. Aamo, Adaptive set-point regulation of linear 2×2 hyperbolic systems with application to the kick and loss problem in drilling, Automatica 119 (2020) 109078.

[36] Q. Gu, A. Fallah, A. Ambrus, Z. Ma, D. Chen, P. Ashok, E. van Oort, A switching MPD controller for mitigating riser gas unloading events in offshore drilling, SPE Drill. Complet. 35 (02) (2020) 201–217.

[37] C. Berg, J.Å. Stakvik, B. Lie, K. Vaagsaether, G.O. Kaasa, Pressure wave propagation in managed pressure drilling- model comparison with real life data, in: Proceedings of the 60th Conference on Simulation and Modelling, Sweden, 2019, pp. 13–16.

[38] K. Gu, An integral inequality in the stability problem of time-delay systems, in: Proceedings of the 39th IEEE Conference on Decision and Control, Vol. 3, 2000, pp. 2805–2810.